AUGMENTING URBAN WIND ENERGY: SHROUDED DIFFUSER CASING FOR ROOF-MOUNTED WIND TURBINES

A Thesis

In the Department

Of

Mechanical, Industrial Engineering & Aerospace Engineering

Presented in Partial Fulfillment of the Requirements

For the Degree of

Master of Applied Science (Mechanical Engineering)

Concordia University

Montreal, Quebec, Canada

October 2017

CONCORDIA UNIVERSITY

School of Graduate Studies

This is to certify that the thesis prepared

By: **Aierken Dilimulati**

Entitled: Augmenting urban wind energy: Shrouded diffuser casing for roof-mounted wind turbines

and submitted in partial fulfillment of the requirements for the degree of

Master of Applied Science (Mechanical Engineering)

complies with the regulation of the University and meets the accepted standards with respect to originality and quality.

Signed by the final Examining Committee:

Dr. Bulgak Akif	Chair
Dr. Luiz A. C. Lopes	Examiner
Dr. Mojtaba Kheiri	Examiner
Dr. Ted Stathopoulos	Supervisor
Dr. Marius Paraschivoiu	Supervisor

Approved by: Dr. Martin Pugh

MASc Program Director

Department of Mechanical and Industrial Engineering

Dr. Amir Asif Dean, Faculty of Engineering and Computer Science (ENCS)

Date: November 7th, 2017

ABSTRACT

The increased demand for renewable energy and the development of energy independent building designs have motivated significant research into the improvement of wind power technologies that target urban environments. However, the implementation of wind turbines in urban environments still faces many challenges. The complexity of wind profile and high turbulence due to the topographical characteristics of urban environments severely limit the performance of urban wind turbines. To explore possible solutions to such challenges and better understand them, the current state of urban wind energy is thoroughly reviewed and the urban flow characteristics are investigated using computational fluid dynamics (CFD). Promising directions that can improve urban wind turbine performance are identified. A flanged shrouded diffuser mechanism - a fluid machine, mounted on rooftop of buildings used as a casing for small wind turbines can significantly improve turbine performance. The fluid machine can increase the wind energy potential by up to a factor of four, by guiding and accelerating the airflow over the building roofs utilizing its geometric features such as, cycloidal curve surface at the inlet and a vortex generating flange at the outlet. The performance of the fluid machine is tested using CFD and wind tunnel tests are also performed. To provide further evidence for its performance, the diffuser mechanism is modeled on the rooftop of an existing building in a test site in Montreal, Canada using CFD and the topographical map including the geometrical data of the buildings in the test site. The CFD analysis performed on the diffuser mechanism in the test site used real statistical wind data of the city of Montreal. CFD investigation of the test site found close agreement with the initially predicted performance of the mechanism. As a power-augmenting device, the fluid machine can mitigate the challenges faced by the urban

wind energy systems and it opens new ways to improving energy efficiency of urban wind turbines.

ACKNOWLEDGEMENT

I would like to thank my academic supervisors and mentors Dr. Marius Paraschivoiu and Dr. Ted Stathopoulos for their support, insight, and guidance in every step of the way. My academic experience at Concordia University as a graduate student has been incredibly valuable and enjoyable because of their support and their efforts in making me a more capable engineer and a researcher.

I would like to thank my colleagues Spencer Foley, Dan McLean, Patrick Larin, Farbod Vakilimoghaddam, Gabriel Naccache, Matin Komeili, Samson Victor, and Jennifer Tan for their valuable insight and feedback on my work. I would also like to thank Hatem Alrawashdeh for his support in the wind tunnel experiments.

I like to take this opportunity to thank Matin Komeili once again for his support and valuable suggestions on my thesis and my research during my master's program.

I met Dr. Marius Paraschivoiu at a CIADI event in 2013 winter when he encouraged me to pursue research as an NSERC undergraduate research student. My academic path has changed ever since. I would not have been where I am today if it weren't for his advice and the opportunities he provided me with to explore both research and the industry and improve myself. I am extremely grateful that I have him as my supervisor and my mentor.

I would also like to thank the Concordia Institute for Water, Energy and Sustainable Systems (CIWESS) and the Natural Sciences and Engineering Research Council of Canada (NSERC) for partial funding of my research through the Collaborative Research and Training Experience (CREATE) program.

TABLE OF CONTENTS

LIST OF FIGURES

LIST OF TABLES

NOMENCLATURE

A	=	Rotor blade swept area (m^2)
A^*	=	Diffuser exit area (m^2)
Cd	=	Coefficient of drag
Cl	=	Coefficient of lift
C_{power}	=	Power coefficient
Cp	=	Pressure Coefficient
C_u	=	k-ε turbulence model constant
C_s	=	Turbulence model constant
C_f	=	Skin friction coefficient
HAWT	=	Horizontal axis wind turbine
K	=	Von Karman constant
$K_{S,ABL}$	=	Equivalent sand-grain roughness height for ABL
Lt	=	Diffuser axial length
L	=	Characteristic length (m)
P_{wind}	=	Wind power (W)
p	=	Building windward face perimeter (m)
R	=	Radius of rotor blades (m)
Re	=	Reynolds number
TSR(or λ)	=	Tip speed ratio
U	=	Wind speed (m/s)
U_{ABL}	=	Atmospheric boundary layer wind speed (m/s)
u^*_{ABL}	=	ABL friction velocity
U_∞	=	Free stream velocity (m/s)
U_τ	=	Frictional velocity (m/s)
VAWT	=	Vertical axis wind turbine
y	=	Coordinate value (m)

y^+	=	Mesh y plus value
Δy	=	Wall first layer mesh height (m)
z_0	=	Aerodynamic roughness
ρ	=	Air density (kg/m^3)
ω	=	Angular velocity (rad/s)
υ	=	Kinematic Viscosity (m^2/s)
κ	=	Von Karman constant
k	=	Turbulent kinetic energy (m^2/s^2)
ε	=	Turbulent dissipation (m^2/s^2)
τ_ω	=	Wall shear stress (N/m^2)

CHAPTER 1: INTRODUCTION

1.1 **Urban wind energy**

Wind energy harnessing technologies are a large part of the renewable energy sector, and as such have been the focus of a great deal of research in the last couple of decades. Developing efficient and cost effective wind turbines for the urban environment is a new area of application that can further reduce dependency on fossil fuels thus reducing greenhouse gas emission. In addition, the ability to provide energy at close proximity to demand, as well as reducing the cost associated with power distribution as a result makes urban wind power a very attractive energy source. The main challenge is integrating wind turbines in complex urban built-environment and building aerodynamics. It is well known that wind power increases with the cube of wind velocity, i.e.

$$P_{wind} = \frac{1}{2}\rho A U^3 \tag{1.1}$$

The velocity and the density of the airflow increases locally in urban areas, as air is forced to navigate around obstacles such as buildings, structures, buses and trains. This creates an opportunity to take advantage of the locally increased density and velocity of the airflow. However, the unavoidable reduction of mean flow due to the increased ground roughness (friction) and the unpredictable - and often changing - direction of air movement, i.e. wind, within urban areas result in a very turbulent flow, which leads to inefficient wind turbines. Therefore, the design of efficient and effective wind turbines, which can operate under these conditions, becomes critical for performance optimization.

1.2 **Overview of urban wind turbines**

The application of wind energy such as, use of wind power to sail ships and wind mills goes back a long time. Persians started using windmills as early as 900 AD (Manwell et al., 2002). Figure 1 shows some ancient Persian windmills. These earliest windmills had vertical rotational axis. Hero of Alexandra, a Greek engineer in the 1st Century AD invented one of the first examples of known windmills, a windwheel that can operate an organ (Drachmann, 1961). Horizontal axis windmills were used in Europe in the middle ages for grinding grains and other mechanical tasks, such as pumping water (Eriksson et al., 2008). Some of the oldest designs of windmills still exist in the Netherlands today. The industrial revolution overshadowed the windmills in Europe while around the same time it became popular in the United States for water pumping applications (Abohela et al., 2013).

Figure 1 Persian Windmills (D'Ambrosio and Medaglia, 2010)

Since the very early attempts to generate electricity using wind by Charles Bush in the United States, 1888 (Eriksson et al., 2008), many different types of wind turbines came to existence based on aerodynamic lift and drag principles, the geometric shapes, and the rotational axis. Wind turbines are classified into horizontal axis wind turbines, HAWTs, and vertical axis wind

turbines, VAWTs, based on the orientation of their rotating axis. Some examples of commercial urban wind turbines are illustrated in Figure 2 for HAWTs, and Figure 3 for VAWTs. The HAWT has improved throughout the 20th century. Its less popular cousin, the VAWT, also became a popular research subject at the beginning of 20th century. The Finish engineer S.J. Savonius invented the Savonius VAWT in 1922 (Peace, 2004). Nine years later, Georges Darrieus proposed the idea of creating VAWT with straight and bent blades, which are called H-rotor and Darrieus wind turbines respectively. Each type of modern wind turbines has different performance profile when integrated into urban based applications. The conventional horizontal wind turbines that offer a relatively more proven technology do not outperform VAWT in urban applications mainly due to the increased turbulent flow. Nevertheless, there are more options and technologies available in selecting HAWTs, and they are more economical but the synergy with the building needs to be evaluated. In built environments, wind speed and direction changes frequently and the unpredictable turbulence makes it difficult for HAWTs to effectively harness the wind energy. HAWTs function well when the rotors are facing the wind flow. However, the HAWTs need to position themselves along wind flow with a tail or yawing mechanism. Early wind power generation in urban environment used HAWTs but the past experience has been disappointing. The primary concept of the different types of HAWTs is very similar. They all use lift forces induced by the incoming wind. The Cd and Cl are the coefficient of drag and coefficient of lift respectively. The tip speed ratio,

$$TSR = \frac{\omega R}{U} \tag{1.2}$$

also, referred to as λ, is the ratio between the tangential speed of the rotor blade tip and the incoming free stream wind speed. The TSR is an important factor when considering turbine power efficiency. The maximum energy generated by HAWTs is limited by the ration of Cd to

Cl and TSR. It determines the angle of attack of wind to the turbine blade airfoil thus affecting resultant aerodynamic forces and torque power.

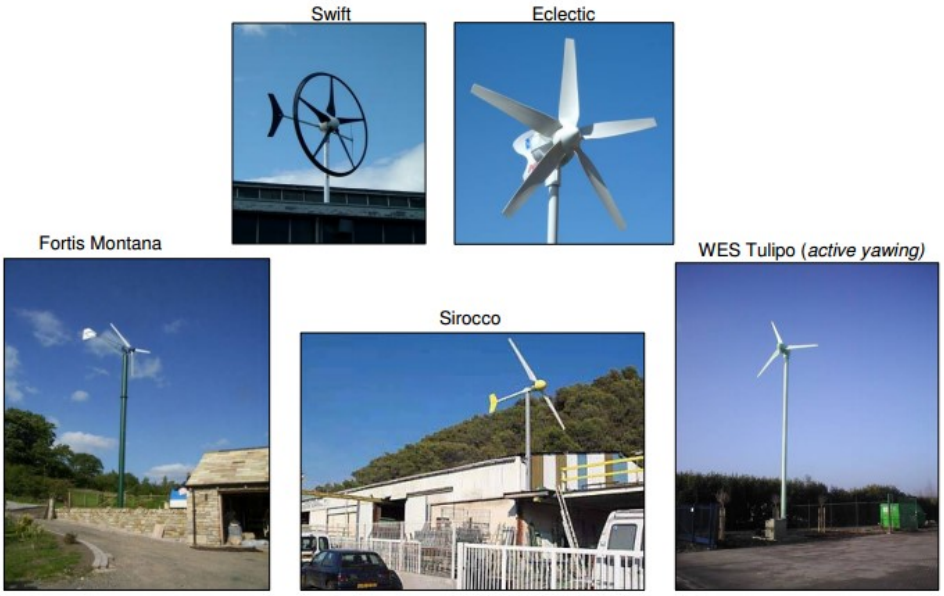

Figure 2 Some examples of commercial HAWTs (Cace et al., 2007)

The VAWTs can also be divided into two categories, lift based VAWTs, e.g. Darrieus type, and drag based VAWTs, e.g. Savonius type. These two wind turbines use different principles to capture wind energy. Savonius, a drag based wind turbine, is popular because it is reliable and easy to manufacture. Wind pushes the Savonius blades using aerodynamic drag forces. The tip speed of the Savonius rotors is generally lower than the wind speed. The Darrieus wind turbines use aerodynamic lift forces to create rotational torque. In this case, TSR is often higher than unity. Darrieus wind turbines are also referred to as H-Rotor or Giromill where the common Darrieus blades are replaced by the straight “egg beater” blades. A few different types of VAWTs in urban environment are shown in Figure 3.

Figure 3 From left to right, Turby, Windside, Ropatec commercial VAWTs (Cace et al., 2007)

The VAWTs rotate about an axis perpendicular to the wind velocity. This characteristic makes them advantageous in environments where wind direction changes frequently and the flow is turbulent. 40 years after Georges Jean Marie Darrieus patented the Darrieus wind turbine, research attention is focused on improving the performance (Macpherson, 1972, Modi et al., 1984, Newman, 1983, Shikha et al., 2005, Tabassum and Probert, 1987, Touryan et al., 1987).

HAWTs are the most common types of wind turbines. However, recent research shows that the vertical axis wind turbines are better suitable for urban applications. The wind flow in urban environment is highly turbulent and multidirectional. The HAWTs are very sensitive to the direction of the wind and do not cope well with turbulent flow and buffeting. Wind tunnel tests at the Delft University of Technology examining the effect of wind approaching from an angle from below revealed that the Vertical helical rotor wind turbines have power coefficient of about 0.4. Due to the 3-dimensional nature of the wind flow, VAWTs are very robust with different directions of wind and better suited for exploiting turbulent flow (Ragheb, 2012). Based on the Wineur Project report (Cace et al., 2007), Table 1 summarizes the advantages and disadvantages of the main types of urban wind turbines.

Table 1 Summary of advantages and disadvantages of urban wind turbines based on Wineur project report (Cace et al., 2007)

	Urban HAWTs	Lift VAWTs (Darrieus)	Drag VAWTs (Savonius)
Advantages	Efficient, Proven technology widely used in wind farms Economical Wide range of commercial product options	Almost as efficient as HAWT at given wind speed Perform well in different wind directions and turbulence Less vibration & buffeting and low noise	Proven products Less acoustic emission Reliable & robust Perform well in different wind directions and turbulence Less vibration Can benefit from turbulence
Disadvantages	Do not cope well with buffeting Perform poorly in changing wind direction	Not yet proven More sensitive to turbulence than drag based VAWTS	Not efficient Comparatively uneconomic

1.3 **Current urban wind turbine designs**

The increasing demand for sustainable building designs and the technological advancement in wind turbine development have created an opportunity for more efficient and realistic wind turbine designs for urban applications. There are many different types of wind turbine designs, each with a unique performance profile. Designs are driven by various requirements specific to the application and location of the device. Some of the design criteria include size constraints, noise limitations, visual disturbance concerns and low start up wind speeds. Depending on these criteria, one particular wind turbine may be more advantageous in one aspect and less in others. Savonius rotors have proven to be well suited to micro-scaled urban operations due to their simple design and relatively low cut-in wind velocity (Saha et al., 2008). The Darrieus vertical axis wind turbine (VAWT) – see Figure 4 (a) - is one of the most attractive options for rooftop

installation, as it is visually unobtrusive and produces low-level acoustic emissions (Balduzzi et al., 2012). In addition, recent designs of Darrieus wind turbines show good self-startup abilities (Batista et al., 2015).

Some wind turbine designs focus more on one particular operational requirement than others. One such example is the Lotus-shaped micro wind turbine that is used in urban applications more for its aesthetic appeal (Yan-Fei Wang and Mao-Sheng Zhan, 2015) - see Figure 4 (b). Relatively, the power generated by a Lotus turbine is not significant, and is usually not the main reason for deployment. The peak power coefficient of the Lotus turbine is less than 0.1. Vertical axis wind turbines (VAWTs) are known to perform well in built-environments due to their multidirectional ability in turbulent flow (Elkhoury et al., 2015). Crossflex, a conceptual design of a building integrated wind turbine using Darrieus VAWT concept was proposed to be integrated to existing buildings (Sharpe and Proven, 2010). The study tentatively validates the advantages of such design over conventional Darrieus wind turbine in terms of its performance and usability. Further research is needed to develop this concept. A photomontage of such turbines is illustrated in Figure 4 (c).

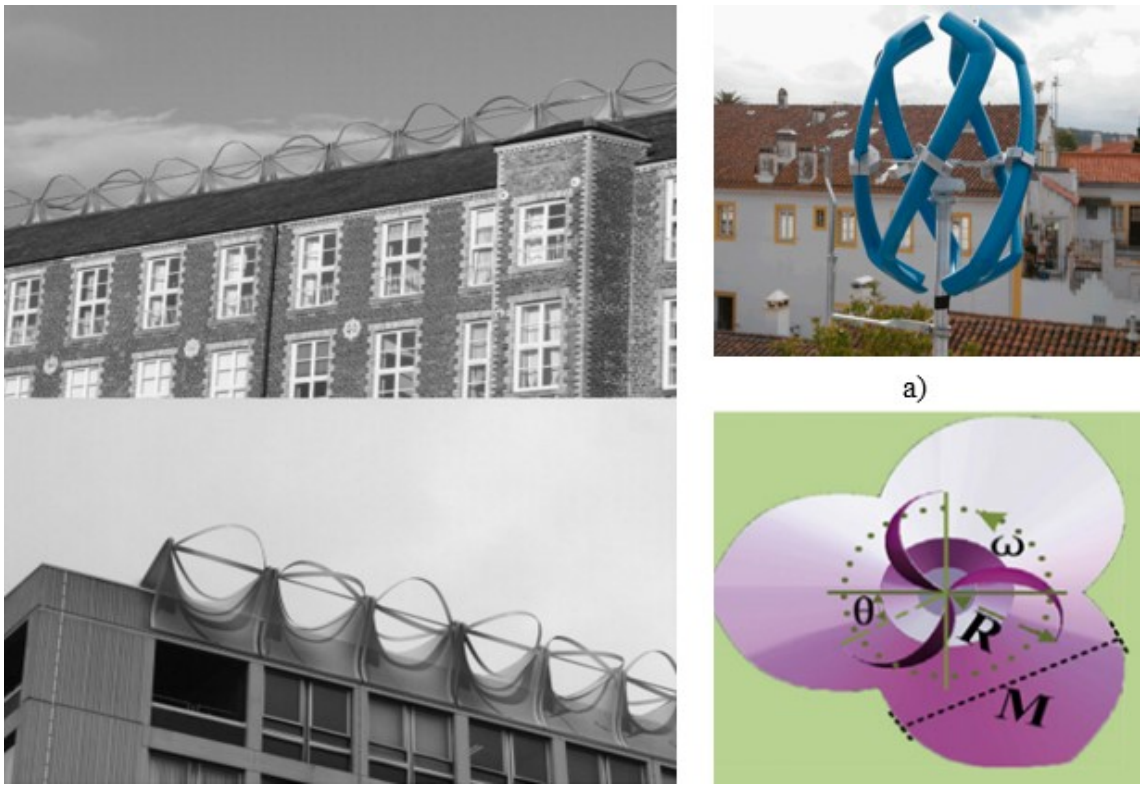

Figure 4 a) From top right in clock wise direction New Darrieus VAWT design prototype (Balduzzi et al., 2012), b) Lotus-shaped micro wind turbine (Yan-Fei Wang and Mao-Sheng Zhan, 2015), c) Photomontage of Cross Flex building integrated wind turbines (Sharpe and Proven, 2010a)

1.4 **Challenges of urban wind power generation and recommendations**

There have been major technological advancements in the development of large-scale wind turbines. Wind turbines in rural terrains and wind farms are presently very efficient. However, the small wind turbines used in urban applications are somewhat under researched. The urban built environment has a lot more restrictions for the wind turbine application than open field installations. A number of human factors, such as, clients, the public, legal and statutory bodies are critical in consideration of the urban wind power generation technologies. Most building-mounted wind turbines in urban contexts are conventional HAWTs with rare examples of VAWTs. The inherent design of these turbines, which was originally aimed at operating in open

fields, makes them less performant in site-specific applications, such as building rooftop, where wind flow characteristics can be very different (Sharpe and Proven, 2010). Turbulence and the constant change of wind direction as a result of morphological complexity of urban architectures present difficulties. The outputs of wind turbines installed on buildings have shown to be extremely low in some field experiments. The turbulence in urban environment contributes to 15% -30% reduction in power output according to Wineur project report (Cace et al., 2007). The average wind power is simply the time average of energy generated over a given period of operation. The capacitor factor is defined as the ratio of average power generated over an operating period to the rated peak power output. Compared to the open field wind turbines which have capacitor factor of 10%, urban wind turbines capacitor factor is only about 4~6.4% according to Wineur project report. The power output of wind turbines is highly unpredictable.

Considering the challenges of urban wind turbines, studies suggest specific recommendations for installation site selection and target buildings. According to the Wineur project and Warwick wind trials (2009), several requirements were found to be critical in ensuring the viability of urban wind power generation. For instance,

- Minimum average wind speed should be 5.5 m/s
- Wind turbines to be installed on a height at least 50% higher than the surrounding structures
- Wind turbines should be installed above the turbulent boundary layer with a specific vertical clearance from the rooftop
- Hub height should be at least 30% higher than the rooftop.

Abohela et al., (2013) suggests that high-rise buildings are better options when selecting buildings for wind turbine installation. The upward inclined wind flow can be exploited by installing wind turbine near the edge of the building where the turbulent layer is relatively thinner. For low-rise buildings, the turbulence effect diminishes as the distance between the surrounding structures and the building is increased. Analysis of the effect of building shapes on wind power has found that among all different shapes of buildings analyzed (domed, gabled, pyramidal, barrel vaulted, and wedged), the barrel vaulted shape proved the best in terms of accelerating wind speed and reducing turbulence intensity in order to efficiently incorporate wind turbines (Nishimura et al., 2014). Further studies suggested that small wind turbines should be installed on towers instead of rooftops of low-rise buildings because the wind speed amplification over the roof of such buildings is relatively lower for energy generation (Lubitz and Hakimi, 2014).

However, Abohela et al. (2013) argues that the viability of urban wind turbines is much higher if proper wind assessments above the target buildings are carried out prior to the installation. Based on their computational fluid dynamics (CFD) analysis, the potential yield of wind power can be increased by up to 56.1% by properly selecting the installation location and the type of building based on its geometric shape. The turbulence effect due to the surroundings is smaller when the target building is taller than the surroundings structures. For optimal wind acceleration and minimum turbulence, the wind turbines should be installed higher off the rooftop.

1.5 **Small wind turbine performance in urban application**

The general implementation of wind turbines in urban built environments is not yet very common. As a result, data available about their performance in real life applications is limited. However, there are several numerical and experimental investigations, both field and wind

tunnel tests (Danao et al., 2013, Kadar, 2012, Rolland et al., 2013a, Rolland et al., 2013b, Roy and Saha, 2015). Currently, power output of urban wind turbines is low. The energy generation of several wind turbines tested for a period of 12 months on rooftops of test homes constructed in the EcoSmart show Village in Chorley, Lancashire, England were below 40 kWh per year when the ratings for these turbines were in the range of 100kWh to 200kWh (Glass and Levermore, 2011). With the energy consumption of inverters, the wind turbines yield almost negative energy output. This was found to be partly due to the inability of wind turbines to cope with the turbulence in urban settings. Urban wind turbines do not generate positive power at wind speed below certain level, the so-called cut-in velocity, i.e. the minimum velocity at which wind turbines start rotating to generate power. Wright and Wood, (2004) investigated the starting behavior of small HAWTs. Reliable and consistent data about urban wind turbine performance in real urban environments is still very limited. A lot of the performance data is either provided by the manufacturers or tested in optimal settings in wind tunnels or even just calculated (Grieser et al., 2015). Urban wind turbines are relatively new in the market. The commercial urban wind turbines often do not deliver their rated power output.

Larger wind turbines perform generally better (Ani et al., 2013) and have more economic efficiency. In principle, the power output of wind turbines is directly proportional to the rotor swept area. However, the experimental results from urban wind turbines show that power generated versus rotor area have almost a quadratic proportionality. Coefficient of power (C_{power}), sometimes referred to as coefficient of performance, is the ratio of power generated to total wind power available, i.e.

$$C_{power} = \frac{P_{generated}}{0.5\rho A U^3} \tag{1.3}$$

This is a critical efficiency indicator. To understand the behavior of turbine at low wind speeds, field experiments were performed for six commercially available micro turbines rated between 0.6 kW to 5.8 kW. Their C_{power}'s are compared for a test site that has a low average wind speed of 3.7 m/s (Ani et al., 2013). Table 2 summarizes the description of these six wind turbines. The peak power coefficients, $C_{power, peak}$, provided by the manufactures – Figure 5 - ranges between 0.2 and 0.56. The field measurements reveal a significantly lower coefficient of power – from 0.10 to 0. 30 – see Table 2 - based on annual amount of energy produced by the turbines. This behavior is quite representative of current wind turbines functioning at low wind speeds.

Table 2 Summary of six commercial urban turbines and their Coefficient of Power calculated from the average annual energy captured by the turbines (Ani et al., 2013)

Turbine name	Fortis Montana	Fortis Passaat	Zephyr Air Dolphin	Ampair	Swift	Turby
Turbine type	HAWT	HAWT	HAWT	HAWT	HAWT	VAWT
Number of Blades	3	3	3	3	5	3
Rotor diameter [m]	5	3.12	1.8	1.7	2.08	2
Swept AREA [m^2]	19.64	7.65	2.54	2.27	3.4	5.3
Coefficient of performance (%) from Manufacturer's data	27.56	17.20	39.57	46.93	24.05	29.08
Coefficient of performance from measured annual energy yields (%)	26.74	14.75	30.14	21.06	13.95	9.79
Difference (%)	4.2	16.6	31.3	122.2	72.4	197.0

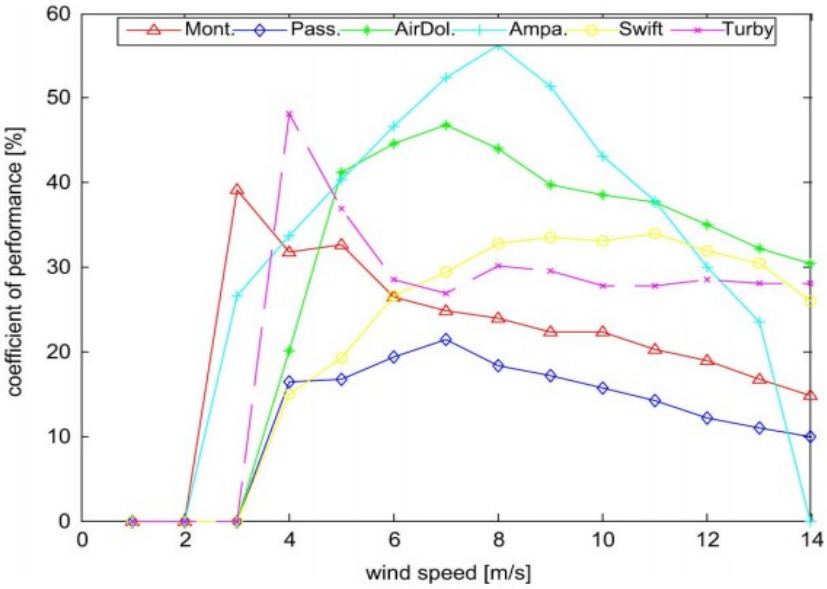

Figure 5 Cp for six commercial urban wind turbines provided by manufacturers (Ani et al., 2013)

Eriksson et al., (2008) shows a comparison of performances of an H-Rotor VAWT, a Darrieus VAWT, and a HAWT. Their efficiencies are compared in terms of their power coefficient. Table 3 shows the maximum C_{power} of these three common wind turbines and the tip speed ratios at the maximum occurs. The data come from different sources (Ashwill and Veers, 1990, Morgan et al., 1989, Muljadi et al., 1998). The H-Rotor extracts more energy at lower wind speed. For a given urban application, the power coefficient is higher for HAWTs than VAWTs at higher wind speed (Eriksson et al., 2008). However, Darrieus wind turbine has a lot of potential to improve and become very efficient considering it is still relatively newer technology than HAWTs. The C_{power} of Darrieus VAWT can be greatly improved by using low drag airfoils (Paraschivoiu, 2002). The Darrieus turbine is competitive with the HAWT as seen in Table 3.

Table 3 Max Cp of three common wind turbines based on data from Eriksson et al. (2008)

	H-Rotor	Darrieus	HAWT
Max Cp	0.38	0.43	0.46
TSR at max Cp	3.8	6	7

Investigation of the performance of two small sized turbines, HAWT and VAWT – see Figure 6, located at the Savona Harbor, Italy is presented by Pagnini et al, (2015). Figure 7 shows the power output measured from January to August 2012 along with the mean velocity measured by an anemometer installed nearby. Two additional anemometer were installed on the turbine structures to measure the exact wind speed experienced by the turbine blades. But the lack of accuracy of wind speed data due to the interference of wake generated by turbine blades and other wind speed recording challenges, the wind speed measured by a third anemometer that is installed nearby is used instead for reference. Initial effort was made to create C_{power} comparison curves for these two turbines for the consistency of this paper. But due to the challenges mentioned above, the exact results of Pagnini et al, (2015) are referenced here to avoid any confusion. It was found that both turbines were extremely sensitive to ambient turbulence conditions, performing well below the rated power output. HAWT is more efficient when wind blows from the sea while VAWT performed relatively better with the wind blowing from the land which has higher turbulence intensity. VAWT experienced much less disturbance and damage from the strong wind gusts (Pagnini et al., 2015). Neither one of these turbines are recommended for installation in complex environments at their current state.

Figure 6 Urban wind turbines: HAWT (right) and VAWT (left) (Pagnini et al., 2015)

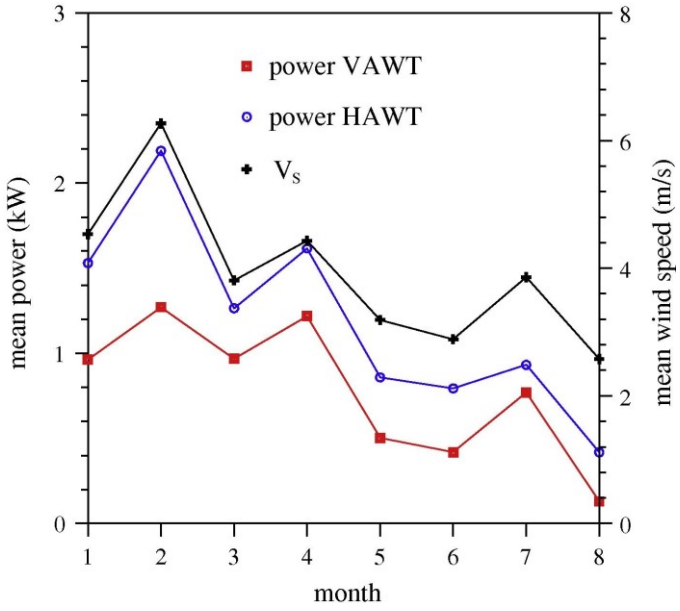

Figure 7 Monthly-averaged power output of two wind turbines (Pagnini et al., 2015)

Table 4 Summary of VAWT and HAWT (Pagnini et al., 2015)

	HAWT	VAWT	Anemometer Vs
Swept Area (m^2)	78.5	46.5	-
Rated Nominal Power (kW)	20	30	-
Installation height (m)	18	23	12.5

Urban wind turbines are still at the early stages of their development. Currently, urban wind turbines are not efficient to provide a viable solution to urban energy needs. Recently, there has been significant research put into exploring the options and improving the existing designs. In fact, energy potential of urban environments is high. A recent study on wind energy potentials and small-scale wind turbine performance at Incek region, Ankara, Turkey, concludes that with the recent wind turbine technologies if implemented appropriately, the entire energy need of an average household in Turkey can be met by wind energy (Bilir et al., 2015). An important development in the field of urban wind energy would be achieved if some of the recently studied designs of urban wind turbines are implemented and the performance validated with more standard experiments.

With the increasing demand for affordable and green energy and with all the technological advancement made in the field of wind turbines, it is important to focus research on implementation of wind turbines in urban settings and improve their efficiencies. Clearly, research shows that there is a wind energy potential in the cities due to the local acceleration of wind over obstacles such as buildings. And if tall buildings which also has high energy demand, can be used to generate and supply some of their energy needs it will make such energy efficient or in some cases energy independent building designs popular making implementation of rooftop wind turbines easier. Currently, wind turbines in urban settings have not gained much credibility. Conventional design and installation setup do not perform well in complex urban environments with highly turbulent and unsteady wind flow. Wind speed and wind directions are very unpredictable and not sufficiently high enough to generate positive energy. There needs to be methods and mechanisms in place to address these issues urban wind turbines have.

1.6 **Literature review of shrouded wind turbines with a focus on urban applications**

To address the challenges of urban wind turbines, such as low average wind speed, turbulence and frequent change of wind direction, research has been focused on shrouded mechanisms that enclose wind turbines. Such mechanisms were found to improve the power output by either re-directing the wind flow to achieve better angle of attack and/or accelerating the wind speed.

Chong et al. (2012) designed an Omni-Direction-Guide-Vane (ODGV) to be integrated with a VAWT for urban applications (Chong et al., 2012, Chong et al., 2013). The guide vanes are nozzles located around the periphery of a cylindrical duct that guides the airflow towards the VAWT. Figure 8 illustrates an ODGV on top of a high-rise building. The torque produced by the wind forces increases by 58% at TSR =2.5 and 39 % at TSR=5.1 (Chong et al., 2013). The ODGV wind turbine also showed very good self-starting abilities. The wind tunnel experimental results show that the bare VAWT wind turbine was able to self-start at wind speed of 7.35 m/s. The same wind turbine, after the integration of ODGV, is found to self-start at 4 m/s. This addresses the previous concern about the self-starting abilities of VAWTs. This improvement on reduced cut-in wind speed also indicates longer operating hours. CFD tests have been performed and validated results obtained from the wind tunnel tests. The power output at the maximum torque with ODGV was 3.48 times higher than that of a bare turbine.

Figure 8 ODGV wind turbine (Chong et al., 2012)

A diffuser augmented wind turbine (DAWT), with a flanged brim structure at the exit periphery of the diffuser, has been tested in wind tunnels, parks and seashores(Ohya et al., 2012, Ohya et al., 2008, Ohya and Karasudani, 2010, Wang et al., 2015). Figure 9 shows a 500W wind-lens turbine used for field experiments in Japan. With a long diffuser length (Lt, the length along the horizontal axis), the brimmed DAWT produces a power output 4~5 times larger than that of a conventional wind turbine.

Figure 9 500W wind-lens turbine (Ohya and Karasudani, 2010)

Figure 10 shows a comparison of the power output of a brimmed type of DAWT (Wind-lens) with that of a conventional wind turbine. The increase in the power output is mainly due to the increase in the mass flow rate as wind accelerates in the diffuser with the low pressure created by the vortex at the exit. The lower curve in green in the figure is the power curve for a conventional "bare" wind turbine. The upper power curve in solid blue is calculated for the predicted improved C_{power} value of 1.4, and the field data match closely with it. The power efficiency of this Wind-lense diffuser HAWT wind turbine is four times higher than conventional HAWT. Skeptics argue that the power coefficient calculated using a smaller rotor blade swept area instead of the total brim area, is misleading. However, the power coefficient is still 40~70% higher for a long diffuser when calculated using the reference area A^*, which refers to the exit brim diameter.

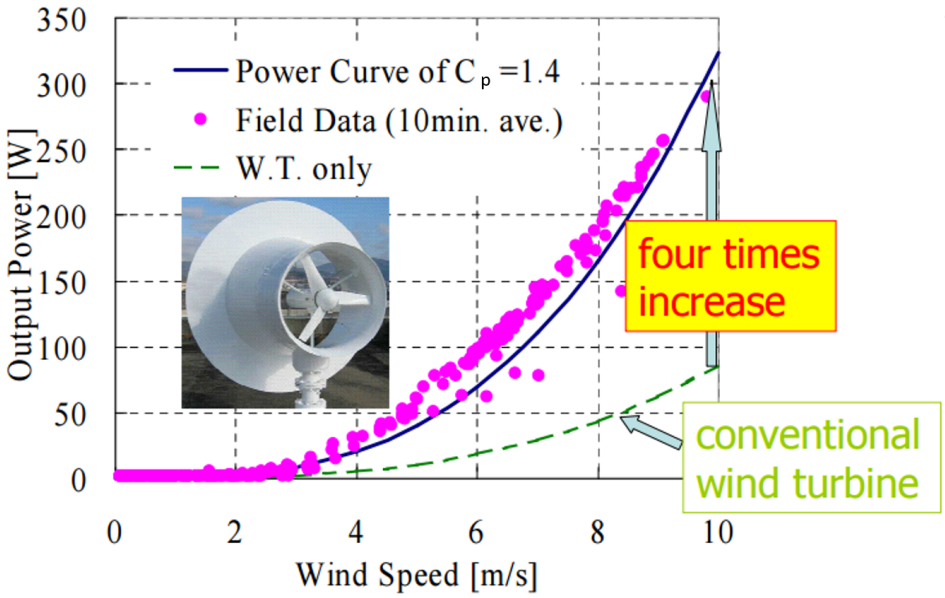

Figure 10 Field experiment of 500W wind turbine with wind-lens *(Ohya and Karasudani, 2010)*

Additional research also investigated the power augmentation effect of brimmed diffuser- wind lens around a wind turbine (Govindharajan et al., 2013). The mass flow rate is increased by at least 15% with the "suction" effect created by the low pressure downstream. The power

coefficient measured using wind tunnel tests is found to be about twice of a typical HAWT. Figure 11 shows a HAWT with a straight diffuser around in a wind tunnel.

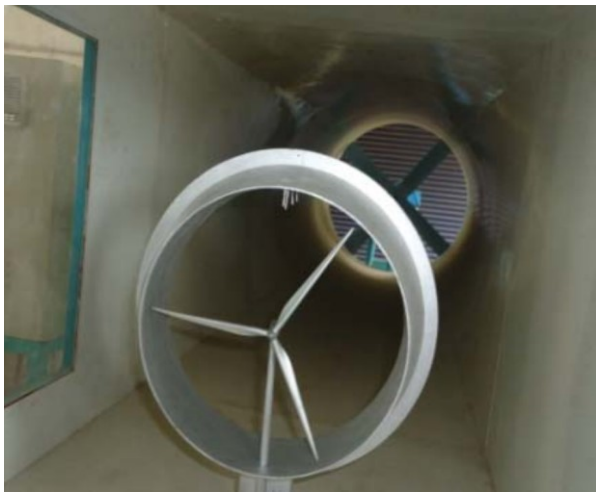

Figure 11 HAWT with straight diffuser (Govindharajan et al., 2013)

A new Building-Integrated Wind Turbine (BIWT) system directly utilizing the building skin is proposed by Park et al., (2015). The system integrates guide vanes on the vertical wall of the building to accelerate wind speed and direct it to the rotor installed inside. Figure 12 (a) shows the proposed configuration of BIWT system. One of the advantages of this system is that it can be used in addition to conventional building integrated wind turbines. Boundary layer wind tunnel test results show that the Savonius rotor inside the guide vane of the BIWT started rotating at a wind speed as low as 1.87 m/s. This is a very low cut-in wind speed compared to most wind turbines. The power coefficient at different wind speeds show a peak C_{power} value of 0.381 at an optimal TSR of 0.55, which is four times better than the conventional bare Savonius rotor efficiency with peak Cp of 0.09 at TSR=0.5 - according to previous experimental results from (Saha et al., 2008). Figure 12 (b) shows a comparison between the power curve of a conventional Savonius wind turbine in dash line with triangular markups for Cp of 0.09, the

power curve of the BIWT for Cp of 0.381 in solid line, and the experimental data points in square markups closely matching the Cp of 0.381 power curve.

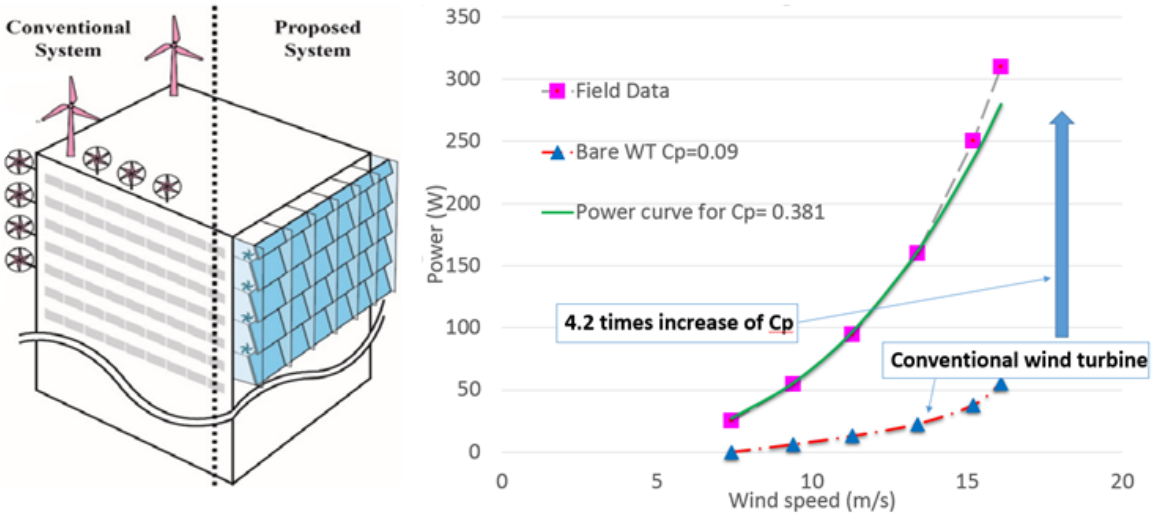

a) b)

Figure 12 a) Building-Integrated Wind Turbine *(Park et al.,* 2015*)*, b) Performance comparison of BIWT based on data from Saha et al. (2008) and Park et al. (2015)

Wind tunnel tests conducted on some other shrouded micro wind turbines also showed a significant improvement on the power coefficient. A HAWT is tested in wind tunnel with and without the addition of diffuser, and a nozzle with diffuser. A simple conical diffuser increased the C_{power} of the HAWT by 60%. The optimal TSR is also increased by 33% with the addition of the diffuser compared to the bare wind turbine (Kosasih and Tondelli, 2012). Given that urban wind is very turbulent, concerns have been expressed about the performance of these shrouded wind turbines in urban settings. However, the experimental results show that shrouded wind turbines perform much better in highly turbulent wind. Although the increase in turbulence intensity affects the power output, the power augmentation is still achieved with the shrouds. Without the diffuser, the power generation drops significantly after TSR of 1.5 at turbulence intensity of 29% (Kosasih and Saleh Hudin, 2016).

Krishnan and Paraschivoiu (2015) designed a new building-mounted VAWT with a diffuser shaped shroud using CFD. A diffuser shaped shroud enveloping a Savonius like wind turbine comprising a number of cylindrical cups was tested numerically. The CFD results demonstrate a C_{power} increase from 0.135 to 0.34. Larin et al., (2016) investigated a horizontal axis Savonius wind turbine placed on the rooftop of a building using CFD. The horizontal axis Savonius wind turbine is dependent on the wind direction and where the turbine is placed on the rooftop as well as the shape of the building. Nevertheless, such optimized wind turbines, taking advantage of the local wind acceleration, can increase the power efficiency up to 0.24. A numerical study conducted by Belkacem and Paraschivoiu (2016) of an array of linear vertical axis Savonius wind turbines also shows promising results in terms of their power output. If the wind turbines are placed in an array normal to the wind direction within 70 degrees range the power output can increase up to twofold.

A CFD investigation of a wind and solar hybrid system – see Figure 13 - that is to be installed on rooftops of buildings by B. Patankar et al., (2016) showed a power output increase of 1.7. The system not only takes advantage of the accelerated wind flow over the building but it also further accelerates and redirects the highly turbulent and otherwise slow wind speeds for wind power generation using vertical and horizontal louvers as seen in Figure 14.

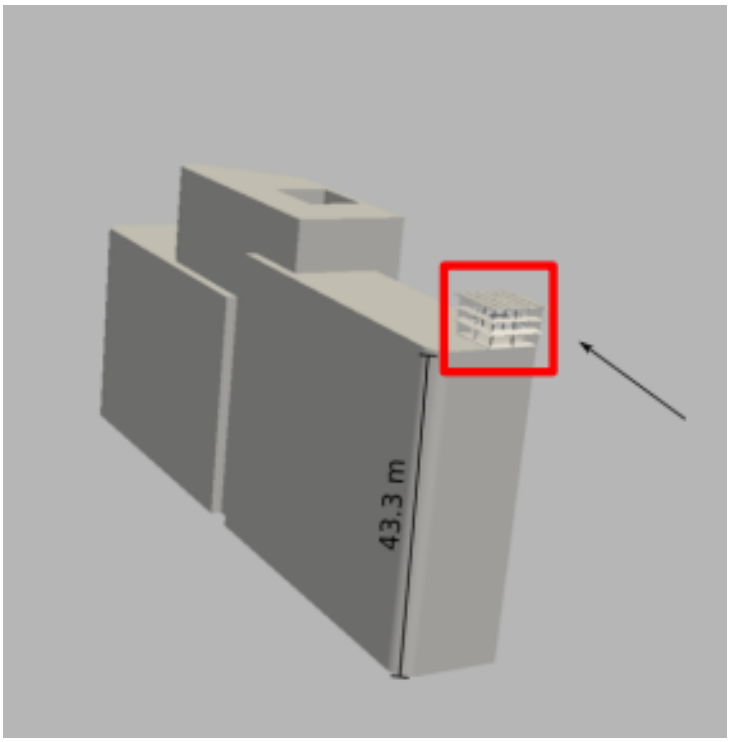

Figure 13 PowerNEST concept on a rooftop of a building

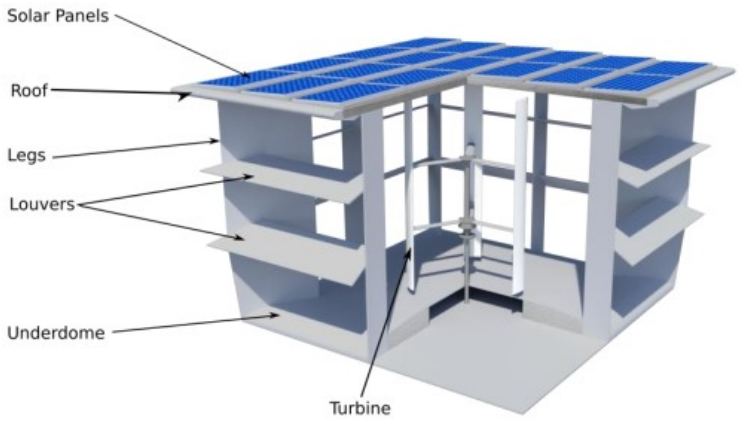

Figure 14 PowerNEST concept with VAWT at the center (Patankar et al., 2016)

1.7 **Motivation**

It is well understood that there is potential to harness wind power in urban environment. But as stated earlier, the urban wind power systems need significant improvement to better take advantage of the available power. To do so, an improved design of wind energy systems that

can improve wind turbine efficiency is necessary. Noting the special characteristics of airflow in the complex topography of the built-environment, it is important to design a system that is compatible with urban applications.

Having to navigate around urban structures such as buildings, wind flow loses much of its power potential making it difficult to harness useful wind energy. However, careful investigation of wind profile over building rooftop sheds light to the possibilities of taking advantage of such urban wind flows. Typically, in built-environment, wind accelerates from the windward side of the building to go over the roof near the roof edge. A diffuser shroud mechanism- see figure 15 - is proposed to be installed on the rooftop to channel the wind flow; further accelerating the wind speed thus augmenting the wind power potentials. And the appropriate wind turbines within the size constrains and tip speed ratio can be installed in the diffuser mechanism to better harness wind energy. Figure 16 illustrates the installation setup of the diffuser on a building rooftop. As previously mentioned, the wind power is cubically proportional to the wind speed. So as much as 25% increase in wind speed can result in double the wind power. Increase in wind speed at the core of the diffuser will also address the low startup wind speed problems. This enables a wider range of turbine selection for a given application. The diffuser also aids in guiding and streamlining airflow from highly turbulent and changing wind speed and direction to a more uniform flow pattern making it easier for wind turbines to utilize the wind flow.

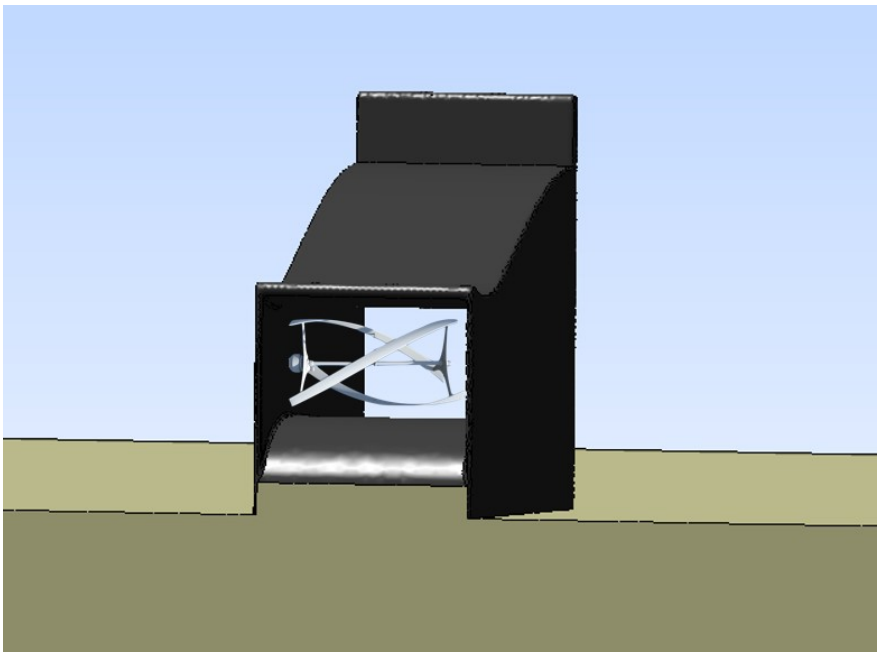

Figure 15 Diffuser shroud mechanism concept with a wind turbine inside

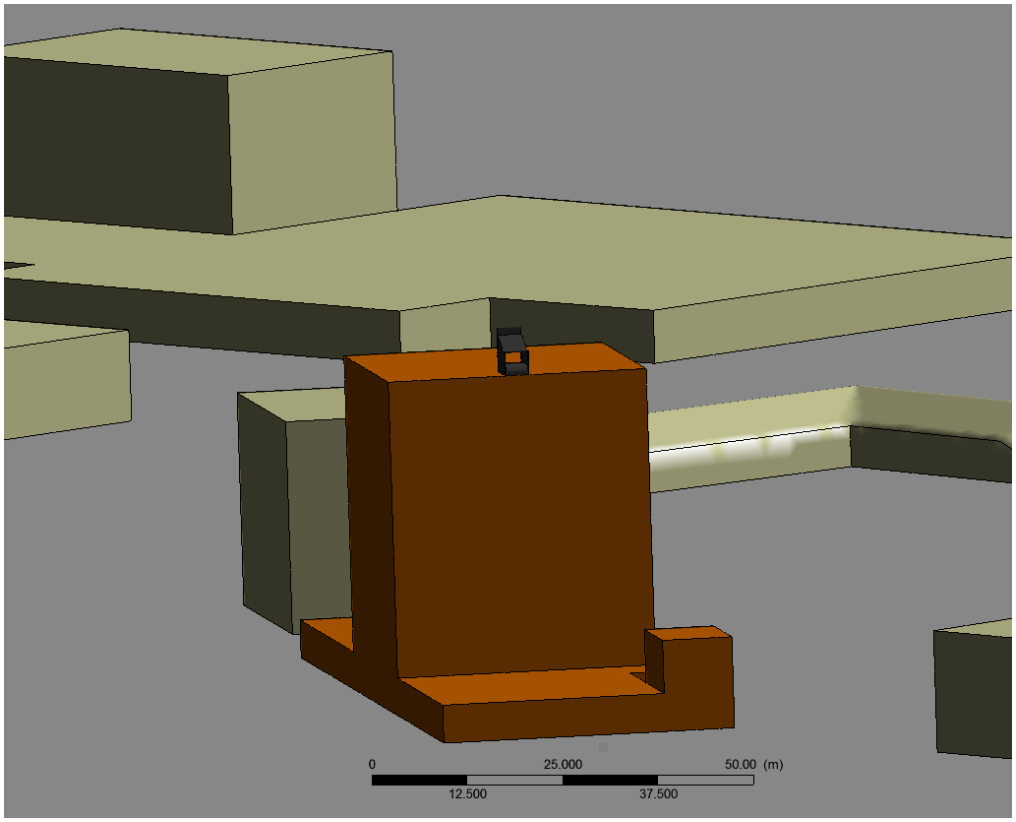

Figure 16 Diffuser shroud mechanism on a building rooftop

1.8 **Objectives and thesis outline**

To address the challenges of urban wind energy technologies and improve the wind turbine efficiency, the proposed diffuser shroud mechanism will be investigated using CFD for its performance such as accelerating and guiding airflow over the edge of buildings. Previous research on shrouded wind turbine performance and CFD results will be the foundation for the preliminary design stage of the diffuser geometry and its positioning on the rooftop.

An in-depth analysis is carried out to obtain preliminary results with the diffuser mechanism on the rooftop of a single building. Comparison of the results with different turbulence modellings and different mesh sizes will be performed to ensure the accuracy of the numerical results.

Wind tunnel experiments with ABL profile is performed to validate the CFD results of the single building case. Once the wind tunnel results and CFD results of the diffuser performance analysis match, further analysis can be carried out to optimize and improve the diffuser's ability to augment wind power in real urban settings with more complex topography.

To characterize to the wind flow in built-environments, two test sites in Montreal Canada is virtually created using CAD and map data. CFD flow analysis is then carried out to better understand the flow properties in the test sites.

The diffuser mechanism's performance is further investigated by virtually modelling it on the rooftop of a real building in one of the test sites with complex wind profile and morphological details. Real wind data obtained from a nearby meteorological site is incorporated into the CFD test to achieve a more realistic result. This stage is valuable in predicting the performance of the diffuser in a real complex urban setting.

The complete analysis involves the following stages:

1. Initial design based on literature review of shrouded casings for wind turbines and preliminary parametric studies on the geometry;
2. CFD investigation of the diffuser's performance and comparison of different numerical setups;
3. Wind tunnel experimental validation of the CFD results;
4. CFD investigation of wind profile in two real test sites in Montreal to examine the urban atmospheric flow characteristics and turbine micro-sitting analysis;
5. Performance analysis of the diffuser mechanism in one of the test sites in Montreal with statistical wind data

CHAPTER 2: METHODOLOGY

This chapter describes the methodology used in this research as well as the different tools employed in every step of the design and investigation processes.

2.1 **Design and test procedures**

For the creation of an efficient, reliable, and robust diffuser shroud casing – a fluid machine, that can significantly improve the power efficiency of urban wind turbines, a series of numerical and experimental investigations are performed to optimize and validate the fluid machine's performance characteristics.

Experimental and CFD analysis are the two main approaches used in this study. Figure 17 illustrates the options considered for the design and test analysis of the fluid machine.

Among the experimental test options considered, particle Image Velocimetry option was not available. Wind tunnel Experiments are performed in the atmospheric boundary layer wind tunnel in the EV building of Concordia University, Montreal, Canada. Scaled down models of the diffuser mechanism are created using 3D printing facility at the EDML machining room in the Hall building at Concordia. The diffuser and building models are assembled along with the wind tunnel instruments in the wind tunnel lab facility.

CFD will be the main tool in every stage of the numerical analysis. Eddy simulation models and Direct Numerical Simulation (DNS) are known to offer the most accurate results but they are not implemented since they are computationally expensive and time consuming. In addition, there are guidelines and best practices, validated with either wind tunnel tests or field experiments, for CFD simulation of ABL flow for only Reynolds- Averaged-Navier-Stokes

(RANS) models. But currently, there is none for Eddy simulation models (Blocken et al., 2015). RANS equations with two equation turbulence models are used in the CFD analysis. For the scope of this task, RANS models are sufficiently reliable within the computational budget. There's significant research that has validated the accuracy and reliability of CFD in designing wind turbines and diffusers. Two equation turbulence models, *k-ε,* Realizable *k-ε, k-ω,* and *k-ω SST* are used in this study. These models have shown accurate results in the simulation of urban wind flow (Prospathopoulos et al., (2012).

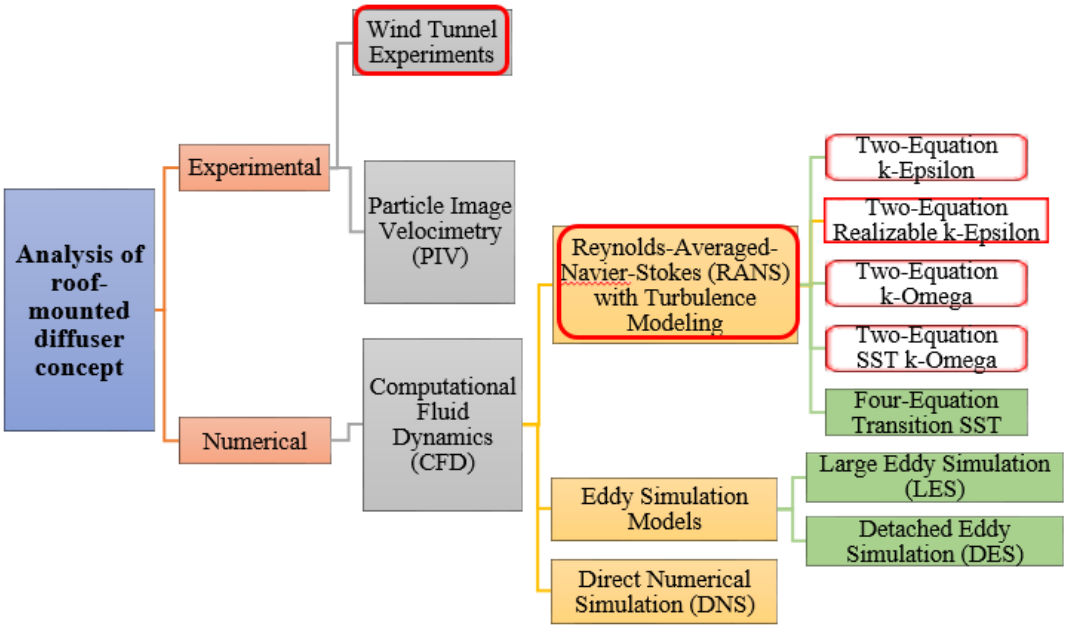

Figure 17 Methodology diagram

2.2 Governing Equations

CFD simulations are performed by solving the discretized Navier-Stokes equations. However, this can be extremely expensive if one wishes to solve the complete Navier-Stokes through DNS simulations. Instead, the time averaged equations, named Reynolds Averaged Navier-

Stokes (RANS), are solved, which offers acceptable accuracy for most engineering applications.

For urban wind aerodynamics, the flow is typically incompressible. The strong formulation of the incompressible and unsteady Navier-Stokes equations for Newtonian fluids are:

$$\nabla.\vec{u} = 0 \tag{2.1}$$

$$\frac{\partial \vec{u}}{\partial t} + (\vec{u}.\nabla)\vec{u} = -\nabla\frac{p}{\rho} + v\nabla^2\vec{u} + f \tag{2.2}$$

where $\vec{u}$ is the velocity vector, v is kinematic viscosity and f is body forces.

The instantaneous flow fields such as velocity and pressure are decomposed into mean and fluctuating components such as

$$u_i = \overline{u_i} + u_i' \tag{2.3}$$

$$\mathrm{p} = \overline{p} + p' \tag{2.4}$$

where u_i and p are the instantaneous velocity and pressure components, $\overline{u_i}$ and $\overline{p}$ are the mean velocity and pressure components, and u_i' and p' are the fluctuating velocity and pressure components. The fluctuating and mean velocity and pressure components vary both in time and space. The subscript i = 1, 2 and 3 refers to the each of the components in the x, y, and z direction, respectively. Using decomposition and some mathematical manipulation, the RANS equation in conservative form are given by the following:

$$\frac{\partial U_i}{\partial x_i} = 0 \tag{2.5}$$

$$\frac{\partial U_i}{\partial t} + \frac{\partial}{\partial x_j}\left(U_j U_i + \overline{u_j' u_\iota'}\right) = -\frac{1}{\rho}\frac{\partial P}{\partial x_i} + \frac{\partial}{\partial x_j}\left(2\nu S_{ij}\right) \tag{2.6}$$

where $-\overline{u_j' u_i'}$ is the average of the product of the velocity fluctuations in the i and j directions, $-\overline{u_j' u_i'} = \tau_{ij}$, called the specific Reynolds Stress tensor, U_i is the mean velocity in the i direction, and S_{ij} is the strain rate tensor

$$S_{ij} = \frac{1}{2}\left(\frac{\partial u_i}{\partial x_j} + \frac{\partial u_j}{\partial x_i}\right) \tag{2.7}$$

Based on the Boussinesq approximation, the specific Reynolds Stress tensor can be express as a product of eddy viscosity,ν_t, and local mean flow strain rate.

$$-\rho\overline{u_j' u_i'} = \rho\nu_t\left(\frac{\partial U}{\partial y} + \frac{\partial V}{\partial x}\right) \tag{2.8}$$

After simplifying the Navier-Stokes equation in conservation form, we obtain the more common expression for the RANS equation.

$$\rho\frac{\partial U_i}{\partial t} + \rho U_j\frac{\partial U_i}{\partial x_j} = -\frac{\partial P}{\partial x_i} + \frac{\partial}{\partial x_j}\left(2\mu S_{ij} - \rho\overline{u_j' u_i'}\right) \tag{2.9}$$

In the above form, there are more unknown variables than equations to solve, meaning the system is not yet closed. The task of turbulence modelling is to find enough equations to solve all the unknowns and solve for the Eddy viscosity variable, which relates the RANS equation with the turbulence model equations through the Boussinesq approximation. In the next sub-sections, the equations for each of the turbulence models used in this thesis are presented.

2.3 **Turbulence Modelling**

In this section, a brief summary of the two equation turbulence models *k-ω SST* is presented. Other turbulence modelling theory and equations are referenced from Ansys FLUENT theory guides.

2.3.1 Shear-Stress Transport k-ω

The two-equation Shear-Stress Transport (SST) k-ω model has a similar form to the standard k-ω model. It combines the benefits of the k-ε model in free flow with the advantages of the standard k-ω for near wall flows. The governing equations are given by the following (Ansys, 2011):

$$\frac{\partial(\rho k)}{\partial t} + \frac{\partial\left(\rho k u_j\right)}{\partial x_j} = \frac{\partial}{\partial x_j}\left(\Gamma_k \frac{\partial k}{\partial x_j}\right) + \widetilde{G_k} + -Y_k + S_k \tag{2.10}$$

and

$$\frac{\partial(\rho\omega)}{\partial t} + \frac{\partial\left(\rho\omega u_j\right)}{\partial x_j} = \frac{\partial}{\partial x_j}\left(\Gamma_\omega \frac{\partial \omega}{\partial x_j}\right) + G_\omega - Y_\omega + D_\omega + S_\omega \tag{2.11}$$

where $\widetilde{G_k}$ is the generation of turbulence kinetic energy due to the mean velocity gradients, G_ω is the generation of ω, Y_k and Y_ω are the dissipation of k and ω due to turbulence, D_ω is the cross diffusion term, and S_k and S_ω are the defined source terms given by the user. Γ_k and Γ_ω are the effective diffusivities of k and ω, and are calculating using the following equations:

$$\Gamma_k = \mu + \frac{\mu_t}{\sigma_k} \tag{2.12}$$

$$\Gamma_\omega = \mu + \frac{\mu_t}{\sigma_w} \tag{2.13}$$

where σ_k and σ_w are the turbulent Prandle numbers for k and ω, respectively; μ_t is the turbulent viscosity called by the following:

$$\mu_t = \frac{\rho k}{\omega} \frac{1}{\max\left[\frac{1}{\alpha^*}, \frac{SF_2}{\alpha_1 \omega}\right]} \tag{2.14}$$

where S is the Strain rate magnitude. The rest of the equations and closure variable are available in ANSYS Fluent's Theory guide (Ansys, 2011).

2.4 **Wall Treatment**

Figure 18 shows the law of the wall, which is the velocity profile in the near-wall region based on a semi-empirical formula. One can see that profile is composed of three regions in the inner layer, which are dictated by the dimensionless distance, y^+. The three regions are the viscous sublayer, buffer region and log law region. The y^+ is defined as

$$y^+ = \frac{\rho u_\tau y}{\mu} \tag{2.15}$$

where u_τ is the friction velocity and y is the normal distance from the wall.

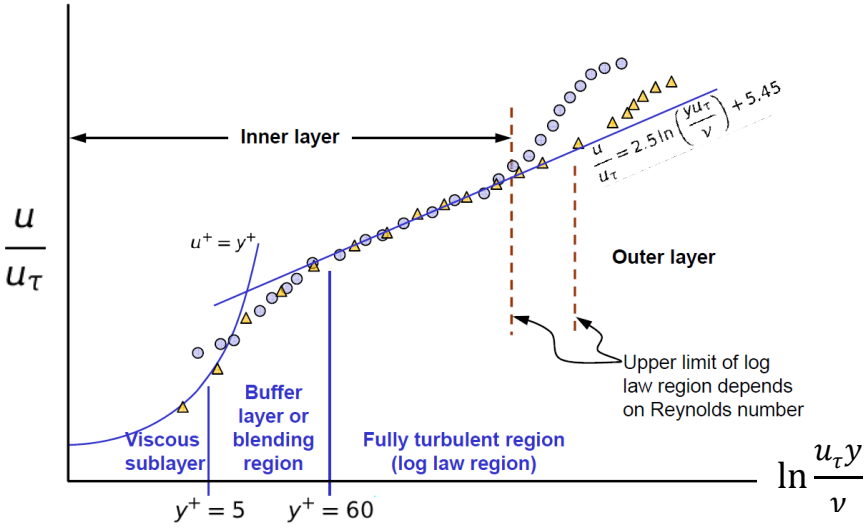

Figure 18 Law of wall (Ansys, 2011)

There are two common approaches of simulating the flow near walls. Wall functions are semi-empirical formulas that bridge the flow between the highly viscous flow in the boundary layer and the free stream flow. The typical range for the smallest element is at $y^+ > 30$, where the flow and its properties below that said y^+ are calculated with the wall functions. If a mesh with elements smaller that y^+ of 15 is used, the flow deteriorates and results in unbound errors. The second approach resolves the flow all the way to the wall, including the viscous sublayer. This obviously requires a much finer mesh to capture the flow details, but typically has higher accuracy in its flow prediction. For Shear-Stress Transport k-ω model, the mesh is resolved near wall to achieve y+ =1. The desired value of y+ is used as input along with the Reynolds number, free stream velocity, density, and viscosity of the fluid to calculate the near wall first layer mesh height Δy using equations 2.16~ 2.20.

$$Re = \frac{\rho UL}{\mu} \qquad (2.16)$$

$$C_f = 0.079Re^{-0.25} \qquad (2.17)$$

$$\tau_w = \frac{1}{2} C_f \rho U^2 \qquad (2.18)$$

$$U_\tau = \sqrt{\frac{\tau_w}{\rho}} \qquad (2.19)$$

$$\Delta y = \frac{y+\mu}{\rho U_\tau} \qquad (2.20)$$

CHAPTER 3: FLANGED DIFFUSER SHROUD MECHANISM FOR ROOF-MOUNTED WIND TURBINES

Previous research demonstrated that a diffuser shroud casing around wind turbines can accelerate wind speed thus increasing wind power (Ohya et al., 2012, Ohya et al., 2008, Ohya and Karasudani, 2010, Wang et al., 2015). A diffuser shroud mechanism - see Figure 17 (a) - is proposed to be installed on building rooftops to channel the upward climbing wind flow and potentially accelerate the flow speed for power generation. Oyha et al. (2010) proposed a similar shroud casing - a fluid machine, that basically consists of a conical diffuser at the core, flow streamlining cycloidal curve geometry at the inlet shroud, and a flange at the exist periphery. Several variations of the geometries have been tested and a compact version of such shroud casing has been patented (Patent number: US 8834092 B2). The flow separation downstream is achieved using a non-streamlining flange at the exit periphery to create annular Karman vortex streets. The low pressure created downstream by the vortices increase the speed of the internal flow. A series of parametric studies of the diffuser shroud geometry and CFD optimization resulted in a geometry that not only guides the airflow but also accelerates the flow speed inside the casing. Figure 19 (a) shows a photomontage of the diffuser with a hypothetical wind turbine inside, while Figure 19 (b) shows the CFD velocity streamlines at the symmetric vertical mid-sectional plane. Instead of the conical diffuser of Ohya et al.'s design, this rooftop shroud casing has a rectangular flow inlet.

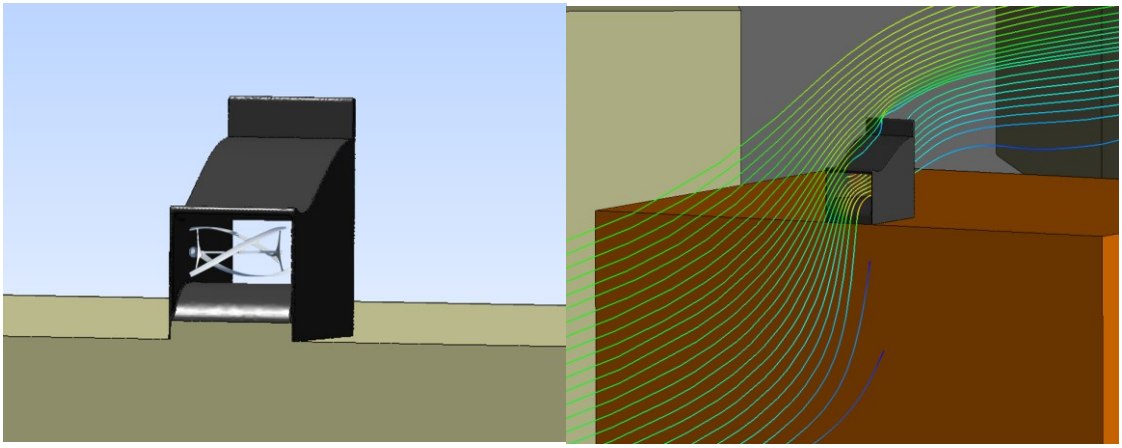

a) b)

Figure 19 Rooftop diffuser shroud mechanism, a) Shrouded diffuser with a wind turbine inside b) velocity streamlines at the rooftop

3.1 **Design progression of diffuser**

Ohya and Karasudani (2010) tested the effect of both diffuser and nozzle as a collection-acceleration device – see Figure 20. Against common belief that nozzle with larger inlet area than the outlet area accelerates air flow as it goes through because of Law of continuity in mind, the experiment found the diffuser more effective in accelerating the flow. The Figure 21 shows the velocity ratio plotted along the axial direction of the devices. The flow "feels" the contraction upstream with pressure waves and avoids the nozzle. On the other hand, diffuser accelerates the flow in the entrances up to 1.8 times of the free stream velocity. Their design of wind-lens technology was mainly used for HAWT on a tower. In this design, similar features will be incorporated into a prismed geometry with rectangular inlet and outlet

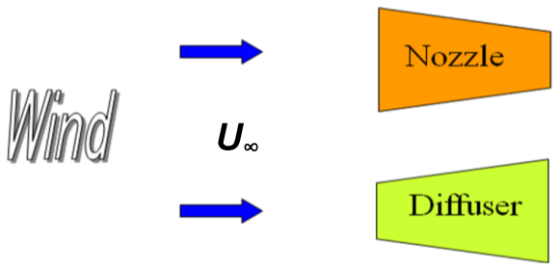

Figure 20 Diffuser and Nozzle and collection and acceleration device (Ohya and Karasudani, 2010)

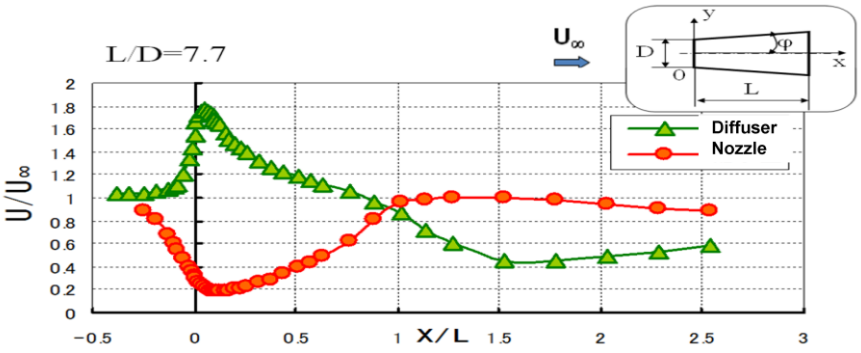

Figure 21 velocity magnification faction of diffuser and nozzle (Ohya and Karasudani, 2010)

3.2 **Parametric study of diffuser for roof-mounted turbines**

Krishnan and Paraschivoiu (2015) have performed some parametric optimization using CFD on a diffuser mechanism installed on the edge of a building. They have tested dimensional parameters such as length, inlet and outlet size, diffuser opening angle, and outlet flange size to optimize the diffuser performance. The outlet flange or brim was added around the periphery of the outlet to create vortices. This low-pressure area at the outlet inhales more air into the diffuser. Figure 22 illustrates the velocity streamlines in the diffuser for different angle of opening on the lower shroud. Shrouds with 0 degree and 5 degrees opening are found to minimize flow separation. The upper shroud inlet kink also creates some flow recirculation compromising the performance of the diffuser. It was also found that reducing the brim height improved velocity magnification.

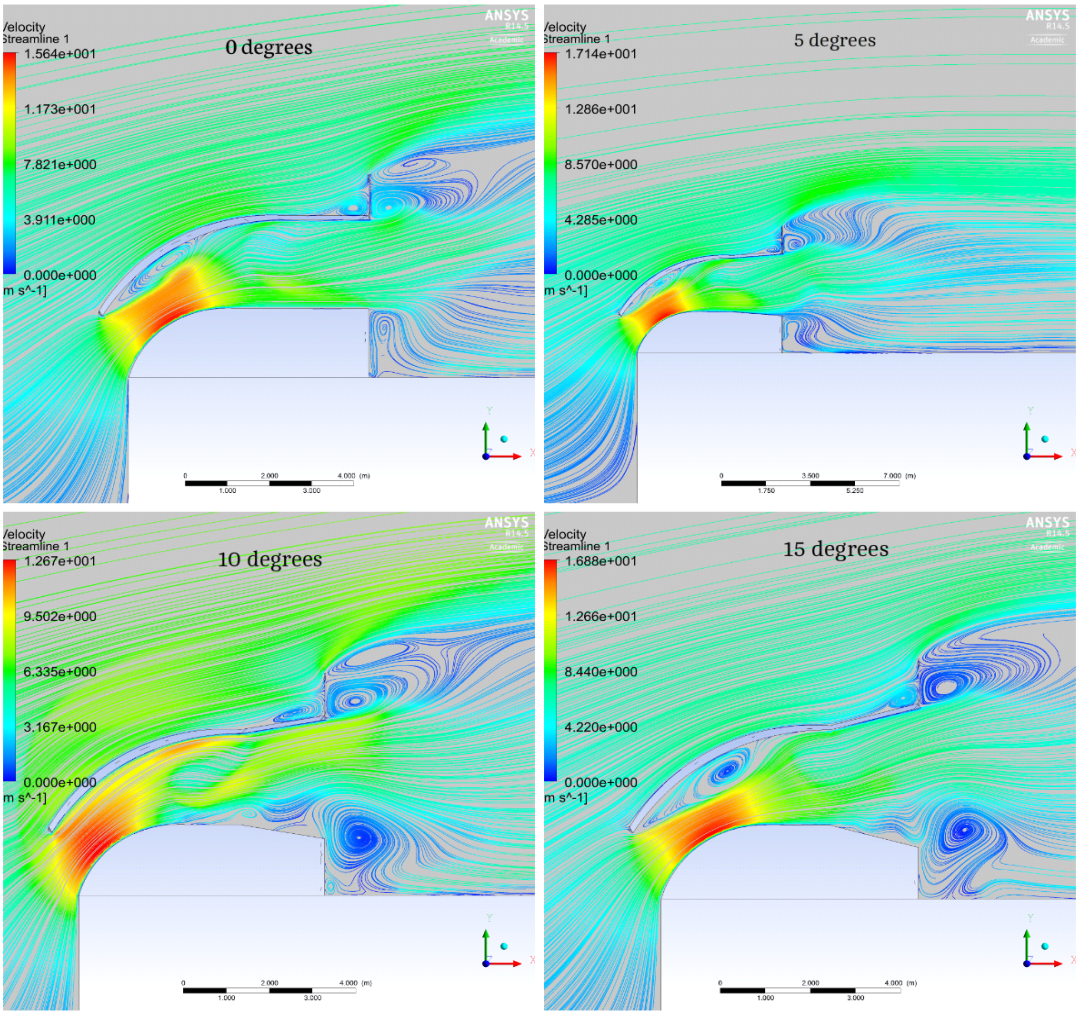

Figure 22 Parametric study of diffuser geometry (Krishnan and Paraschivoiu, 2015)

For the inlet shroud geometry, cycloidal curves are used to create the surface. The cycloid curves are generated using the Equations 3.1 and 3.2. Figure 23 illustrates the geometric pattern of cycloidal curve. Ohya and Karasudani (2010) found the cycloidal geometry to perform well in streamlining the flow along the inlet shrouds. The convex portion of a cycloid curve is implemented at both upper and lower shroud of the inlet to create streamlined flow and low pressure at the outlet to draw more air. The geometry of the wind-lens technologize that uses the cycloidal geometry is patented by Ohya et al (Patent number: US 8834092 B2)

$$x = r\,(t - \sin t) \tag{3.1}$$

$$y = r\,(t - \cos t) \tag{3.2}$$

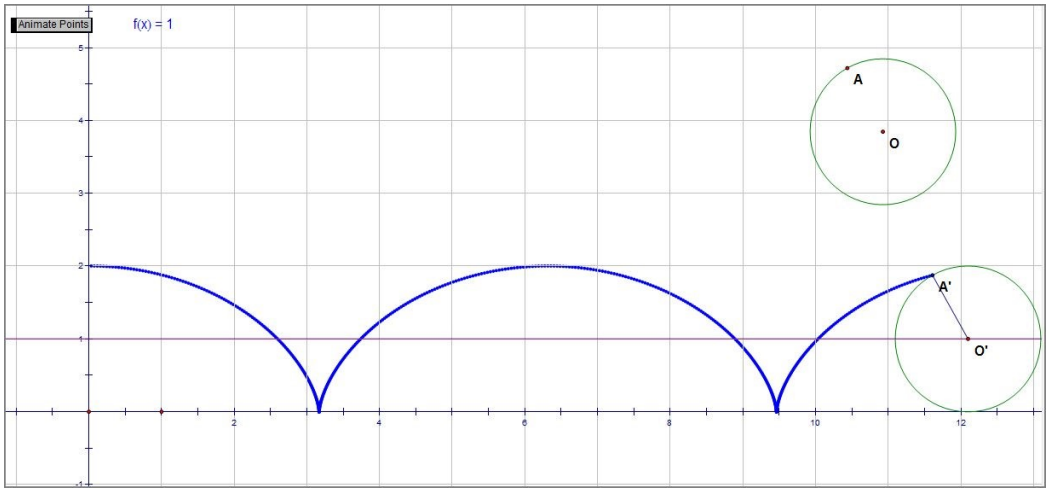

Figure 23 Cycloid curve

An aspect ratio of 1:1 is selected at the inlet opening. This corresponds to an aspect ratio of approximately 2:1 of at the throat of the diffuser where the turbine is to be installed. Increasing the aspect ratio of the inlet opening, such as wider inlet opening, may increase the range of azimuthal angles that the diffuser can be used to draw air. But for the purpose of wind turbine installation at the throat, too wide of an opening may not be practical. The boundary layer on the top and bottom surfaces, and the diameter of the wind turbines may be negatively affected by larger aspect ratio. Perhaps, case specific studies on the aspect ratio with a particular turbine geometry will be more appropriate.

Based on the preliminary parametric test of the diffuser geometry, the following geometry – see Figure 24 - is created for further analysis on a building rooftop.

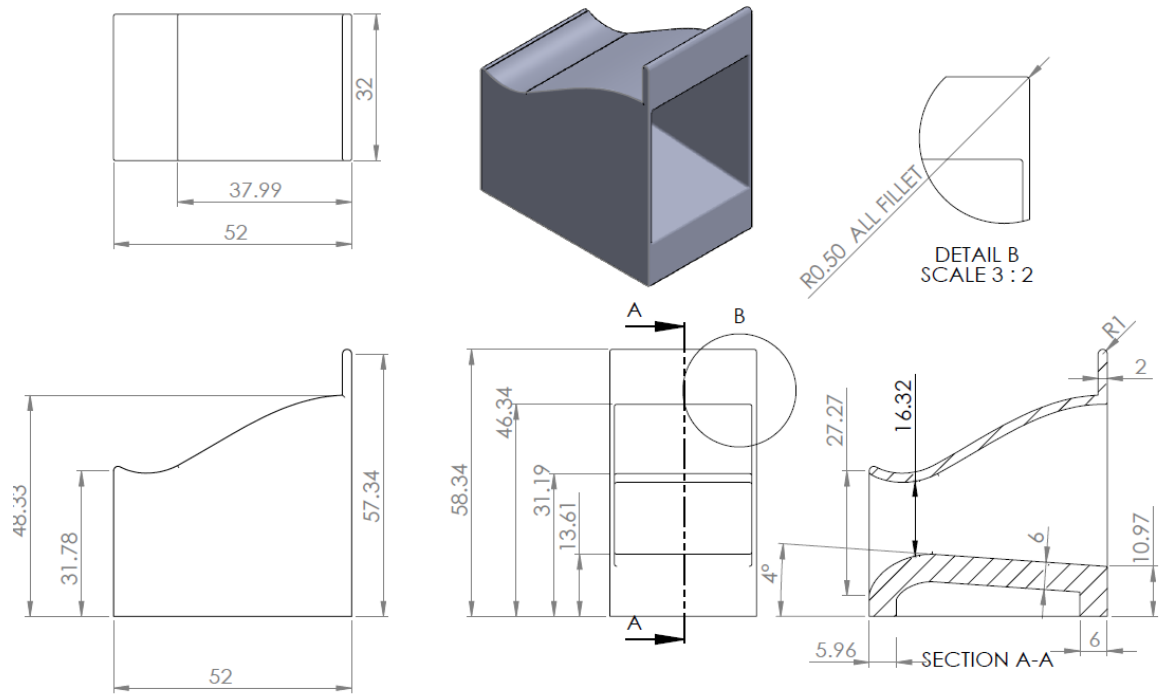

Figure 24 Diffuser geometric details, units in (mm)

CHAPTER 4: CFD INVESTIGATION OF DIFFUSER PERFORMANCE

In this chapter, the diffuser shroud geometry will be tested with a single building using CFD to examine its performance and compare the results with different turbulence models, boundary conditions, and mesh sizes.

4.1 **Domain and boundary conditions**

The diffuser shroud is modeled on the rooftop of a flat-roofed building with dimensions, 16 m × 16 m × 28.45 m (W × L × H). Ledo et al. (2011) found that flat-roofed buildings are best for roof-mounted wind turbine deployment. Half of the physical domain is constructed to save computational costs by setting the mid-sectional plane as a symmetry boundary condition. H is the height of the building. The domain extends by 3H of a length upstream of the building, 11H downstream totaling approximately 15H from inlet to outlet, 3H in lateral direction, and 4H in vertical direction – see Figure 25 - to achieve "horizontal homogeneity", i.e. the absence of stream-wise gradients in vertical profiles of wind speed and turbulence quantities (Blocken, 2015). Horizontal homogeneity implies that the inlet profiles are identical to approaching flow profiles and incident profiles (Blocken, 2015). The downstream of the domain is created far enough to avoid any pressure wave reflection from the pressure outlet. All solid surfaces are modeled as no-slip wall conditions. The inlet is set as atmospheric boundary layer (ABL) velocity inlet, the outlet as pressure outlet and the mirror face, top and sides are modeled as symmetry boundary conditions. Other CFD setup is as per the best practices based on benchmark experiments of CFD used in urban wind engineering by Blocken et al., (2004) and the recommendations by Franke et al., (2011).

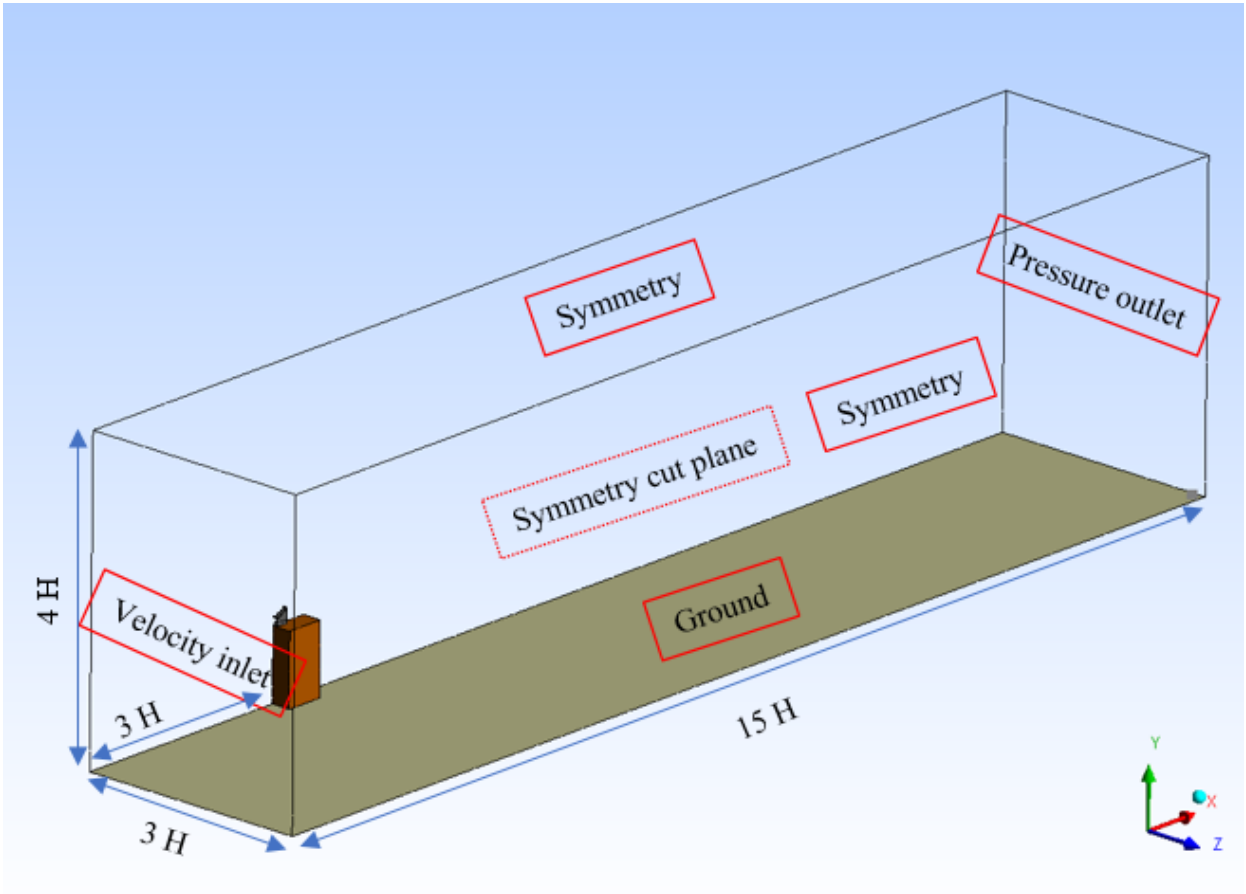

Figure 25 CFD test domain

4.2 **Turbulence model comparison**

3D steady state RANS models are selected for this analysis. There are limitations with steady state analysis of turbulent flow yet it is widely used and acceptable in research (Blocken et al., (2004). It is also recommended to use RANS models for CFD in urban wind engineering; for two main reasons, one, the cost associated with the computational process and the topographical details needed for large eddies simulation (LES), two, the lack of standard best practices and guidelines for the use of other turbulence modeling specifically for urban wind engineering. Currently, there are guidelines for modeling urban wind using CFD to address complex profile of wind such as turbulence in built environment.

The CFD tests are conducted for *k-ω, k-ε* using standard wall functions, and Realizable *k-ε* turbulence, *k-ω* SST models. Karava et al., (2011) recommends the use of Realizable *k-ε* turbulence modelling for urban wind flow in general to address the sharp pressure gradient and flow shear layer in the ABL flow as well as the eddies and the recirculation. *k ω* SST is also widely used for its superiority in capturing flow that involves adverse pressure gradient and flow separation. Therefore, *k-ω* SST is used to better understand the flow characteristic as air flows over the curvature of bottom shroud to accurately predict the adverse pressure gradient it experiences.

4.3 **Mesh grid sensitivity**

Figure 26 (a) shows the building and the diffuser mesh. Different mesh grids are used for *k ω* SST and for other three models to address the differences in the requirement of wall function parameters such as y+. Fine inflation layers are created on the diffuser surfaces to achieve y+ value of one – see Figure 26 (b). The grid sensitivity is investigated by using two different mesh sizes to evaluate the solution and compare the results while keeping all else the same. The goal is to achieve a mesh independent solution as it should be since the physics of the problem does not depend on the mesh resolution. Finer mesh has 20% more elements in the domain than the baseline. Table 5 shows the velocity magnification factor for two different mesh sizes. The mass-weighted averaged velocity of air at the diffuser throat is compared to velocity upstream at the same elevation. Figure 27 shows the location of the diffuser throat in red where the velocity is measured. Ideally if the solution is entirely grid size independent, the results for the velocity magnification factor should be the same. The finer mesh prediction of velocity magnification differs from that of the baseline mesh by 3.3%. The difference is acceptable. The information about the baseline mesh used for *k ω* SST turbulence model is shown in Table 6.

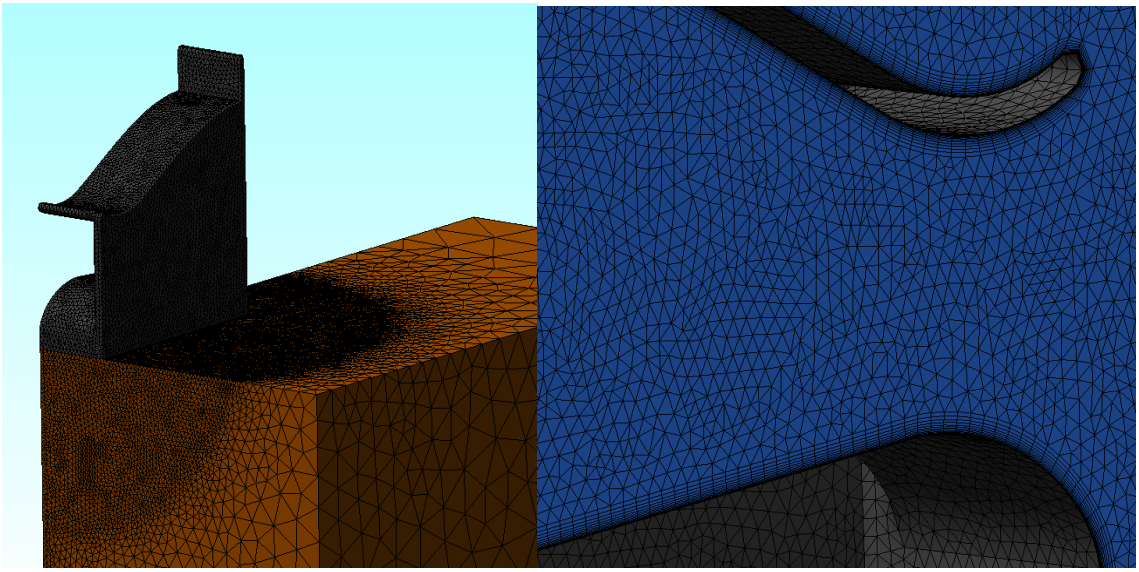

a) b)

Figure 26 a) diffuser and building mesh, b) surface inflation layers

Table 5 Mesh Grid comparison

Mesh grid	$\frac{U}{U_\infty}$
Baseline	1.52
Finer mesh	1.57

Table 6 Baseline mesh information

Number of Nodes	8024419
Number of Elements	3737925
Tetrahedra	3276947
Wedges	459361
Pyramids	1617
Hexahedra	0
Polyhedra	0

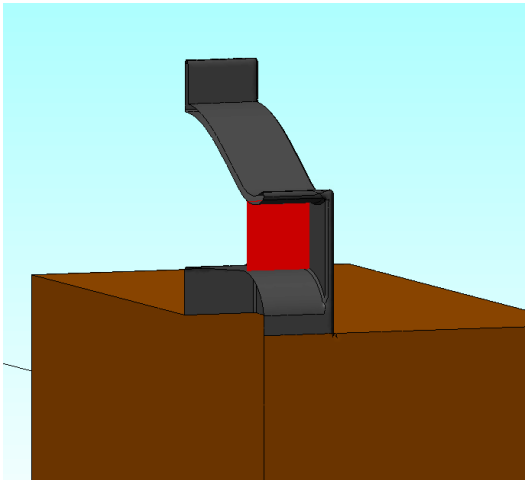

Figure 27 Diffuser throat location

4.4 **Results and discussion**

Table 7 summarizes the calculated velocity magnification factors at the throat obtained from different turbulence models. Figure 28 illustrates the velocity contours and velocity streamlines at the diffuser for *k-ω* SST turbulence model. The airflow has the tendency to move upwards inside the shroud. But the streamlines show that there is no significant separation of the flow or recirculation in the diffuser. There is however recirculation just at the exit of the outlet. But this is similar to Ohya's Wind-lens technology and patent where the Karman Vortex streets downstream is used to create low pressure thus drawing more air into the diffuser. Realizable *k-ε* turbulence model predicts very similar result as *k-ω* SST with 2.2% difference. Figure 29 a) and b) shows the velocity contour of Realizable *k-ε* turbulence model and *k-ω* model respectively. *k ω* model also predicts the velocity magnification factor quite closely with 5 % difference compared to *k-ω* SST. The *k-ε* turbulence model on the other hand predicts a somewhat distinct flow profile with 14% difference. Figure 30 illustrates the velocity contour using *k-ε* turbulence model. As the airflow goes around the "bend" along the stream-wise direction near the bottom shroud the boundary layer grows and the flow experience relatively

high adverse pressure gradient. The k-ε turbulence is best for solving flow far from the wall. But it is not the best option to analysis flow characteristics in this case.

Table 7 Velocity magnification factor with different turbulence models

Turbulence Models	Velocity magnification factor $\frac{U}{U_\infty}$
k-ε standard wall function	1.56
k-ω standard wall function	1.30
Realizable k-ε	1.40
k-ω SST	1.37

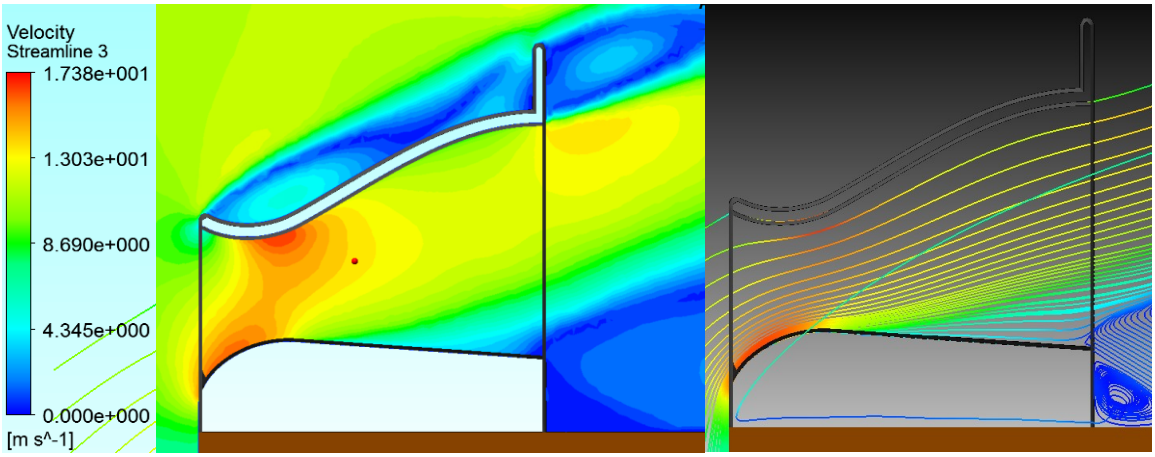

b)

Figure 28 a) velocity contour and b) velocity streamlines for k-ω SST

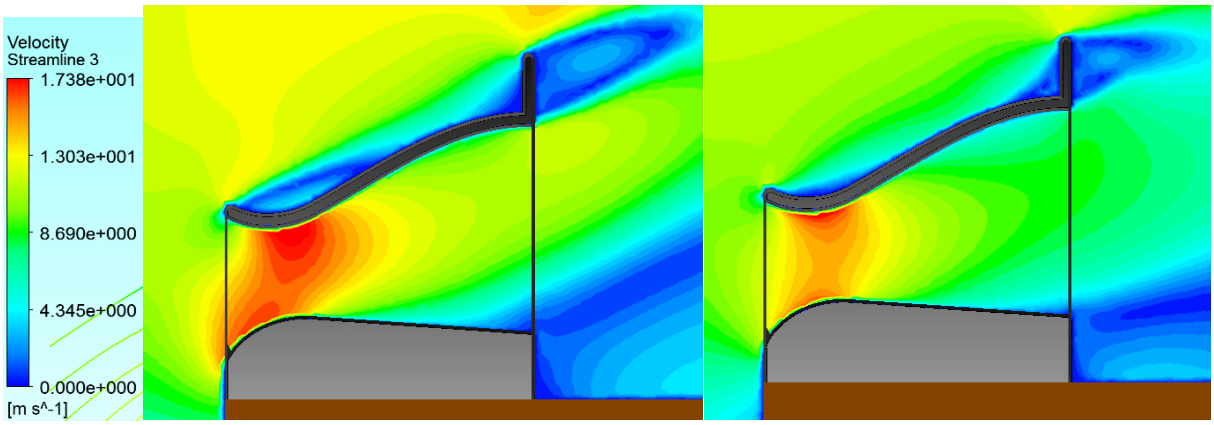

a) b)

Figure 29 Velocity contour for a) Realizable *k-ε* turbulence model and b) *k-ω* model

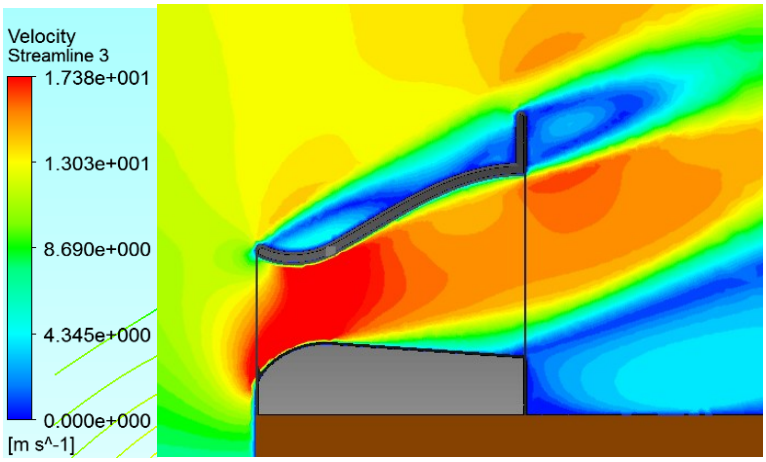

Figure 30 Velocity contour for *k-ε* model

Previous CFD analysis including the parametric tests on the diffuser geometry has predicted relatively higher peak velocity at the diffuser throat with magnification factor of 1.6 using *k-ω* turbulence model with standard wall function. However, in these cases only ABL velocity profile is incorporated in the velocity inlet boundary condition with default turbulent intensity of 5 % and turbulence viscosity ratio of 10 instead of a ABL turbulence profile. There is a clear difference in the results. The complexity of urban wind profile including turbulence profile is an important factor in the velocity profile of the flow. The exact flow characteristics may very well be case specific with the location's morphological structures and the airflow structures of

the region. Therefore, the results shown here should be used as a proof of concept but not as an absolute value. The exact values of velocity magnification factor depend on the structure of the building with respect to the local wind profile and geometric scales. Once again this proves the importance of a thorough assessment of turbulence and flow profile of the siting location prior to the deployment of urban wind turbines.

4.5 **Characteristics and performance of flanged diffuser shroud**

CFD tests with the ABL flow conditions show that at the throat of the diffuser, the wind velocity can accelerate up to 1.6 times of the upstream velocity at the same height. The increase in velocity indicates that using such mechanisms, the wind power can be significantly increased, as much as four times compared to a conventional wind turbine installed on a turbine tower of the same height. This also helps turbines operate for longer hours by easing the limitation of low cut-in wind speed. Figure 31 (a) and (b) show the diffuser sectional view with the velocity streamlines. The flanges at the exit of the shroud, like Ohya et al.'s power augmentation method, draw more air into the diffuser by creating suction downstream. The cycloidal curves used at the entrance on both upper and lower shrouds improve the streamlining and guide the flow towards the diffuser throat where the turbine is to be installed. In addition to its ability to guide and accelerate the airflow, the diffuser mechanism addresses some of the common problems urban wind turbines have and offers advantages such as,

- Increased safety reducing contact between rotating turbine blades and the external objects, debris and animals
- Containing broken pieces of turbine blades from shooting out to public areas in case of damage

- Reducing noise from the turbine blades as fluctuating vortices generated by the blades are suppressed within the boundary layer on the internal shroud surfaces
- Eliminating visual disturbances as the moving parts of the turbine are hidden inside the solid casing
- Providing potential surfaces for solar panels or similar hybrid power systems
- Providing a braking mechanism by closing the inflow.

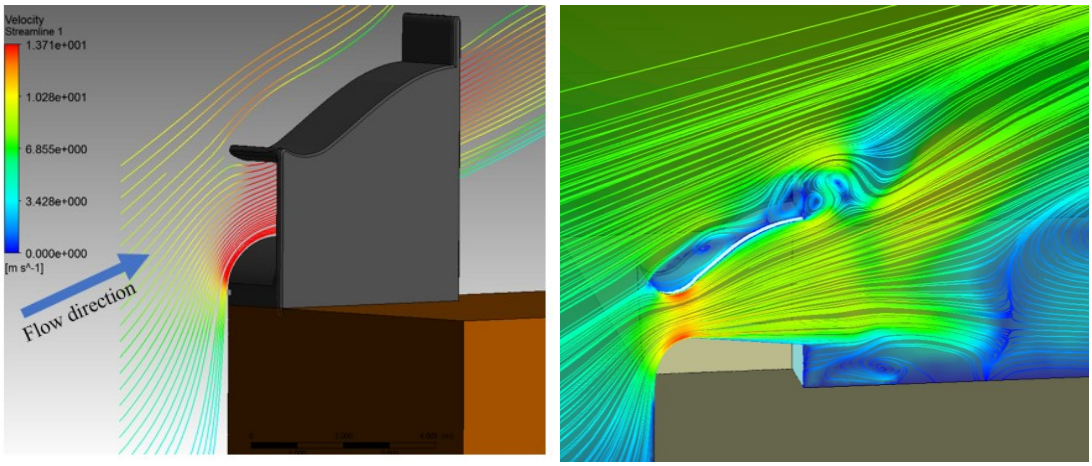

a) b)

Figure 31 a) Rooftop diffuser shroud mechanism with velocity streamlines b) symmetric cut view of velocity streamlines

CHAPTER 5: WIND TUNNEL TEST

5.1 **Wind tunnel model**

An atmospheric boundary layer wind tunnel at Concordia University in Montreal, Canada – see Figure 32 (b) - is used to validate the CFD results of the diffuser performance with a 1:100 scale model of the diffuser on top of a building 16 cm × 16 cm × 28.45 cm (W × L × H). Velocity and turbulence profile of the wind tunnel is measured and used as the boundary conditions for the CFD simulation. Pitot tube in the gradient height of the ABL flow and static pressure taps installed on the bottom shroud of the diffuser – see Figure 32 (a) - are used to calculate the pressure coefficient, Cp. Cobra probe, an instrument that is capable to measuring mean velocity and velocity fluctuations in 3 directions is also used. Measurements of these six values are taken at 3H upstream location (H is the building height) of the test building. Twenty-point data along the vertical direction is taken to curve fit the ABL flow profile such as, velocity and the turbulence quantities. k, ω, and ε are calculated from the Reynolds stress based the measured velocity fluctuations. These curve-fitted functions were used as boundary conditions in the previous CFD validation stage so the wind tunnel results can be compared more accurately with the boundary conditions.

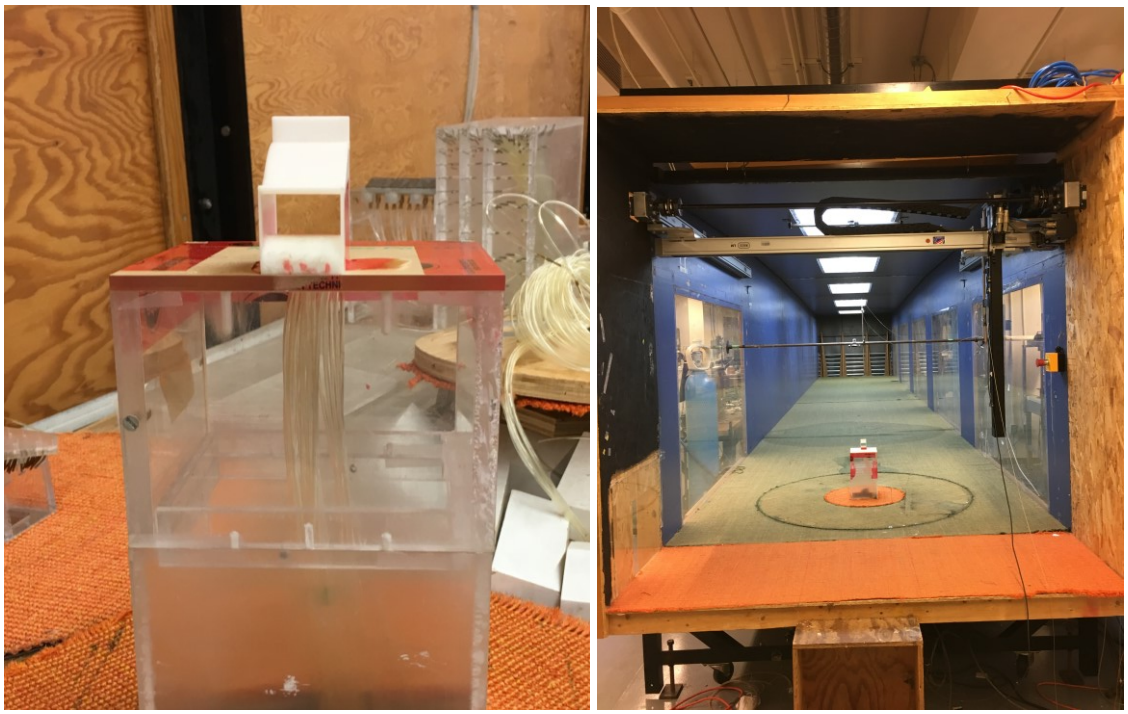

Figure 32 a) Diffuser mechanism with pressure taps b) Diffuser on a single building rooftop in a wind tunnel

5.2 **CFD and wind tunnel result comparison**

The wind tunnel is 12 meters long, 1.7 meters high with 1.8 width. The model building is 0.2845 meters tall with the blockage ratio of 0.0158. It is recommended to keep the blockage ratio below 5% in the wind tunnel. The geometric similarity must be maintained to analyze the flow over the building since the flow profile over the edge is crucial for the diffuser performance. The diffuser has an inlet opening less than a few centimeters. Cobra probe is too large to be used for velocity measurement inside the diffuser at this scale. Any larger scale will have too much of a blockage ratio. So instead. the static pressure taps are used to validate the CFD methods. And if the pressure coefficient comparisons of CFD and wind tunnel are successful, then confidence will be gained about the CFD prediction of flow velocity magnification as the result of the diffuser.

5.2.1 Effect of Reynolds number in the flow profile

Reynolds number similarity is important. Reynolds number is the ratio of inertial forces to viscous forces and it is defined as,

$$Re = \frac{UL}{v} \quad (5.1)$$

Where:

- L is a characteristic linear dimension (m), Note that the building dimensions are used to calculate the L= 0.205 m, ($L = \frac{4A}{p}$, where A is the wind facing area of the building and the p is the perimeter of the face)
- U is the velocity of the fluid with respect to the object (m/s), the velocity of air upstream at the diffuser elevation is 12.5 m/s
- v is the kinematic viscosity of the fluid (m^2/s), the kinematic viscosity of air is 15.11×10-6 m^2/s

CFD investigation of the effect of Reynolds number variation due to the different geometric scales shows that at the smaller geometric size or lower Reynolds number for that matter, the flow separates as it goes around the convex part of the bottom diffuser shroud – see Figure 33 (a). As the Reynolds number decreases the flow starts to separate at the bottom shroud. Figure 34 illustrates the flow separation effect with varying Reynolds number. At the 1:100 scale or Re = 170 000, the flow separates almost immediately after the entrance – see Figure 34 a). This can be explained by the prevailing viscous forces at the lower Reynolds number creating severe adverse pressure gradient at the curvature of the bottom shroud resulting in flow separation. With the full scale previously optimized for the diffuser performance which is around 5 meters

in length at Re= 17 million (Note that Reynolds number is calculated with the characteristic length of the building not the diffuser) – see Figure 34 c), the flow pattern is ideal for diffuser performance. CFD predicts that the flow separates at lower Reynolds number which is the case in the wind tunnel test – see Figure 33 a) velocity contour b) velocity streamlines- showing the flow separation and the secondary flows at the bottom shroud after some inlet distance.

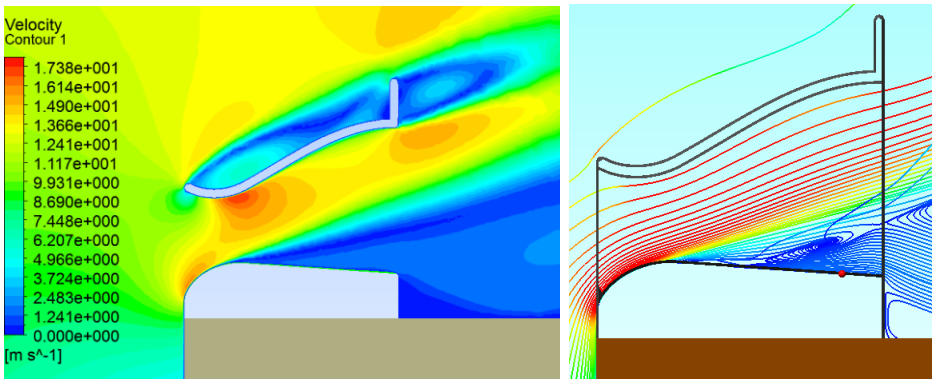

Figure 33 CFD velocity contours of wind tunnel geometry at a) velocity contour b) velocity streamlines

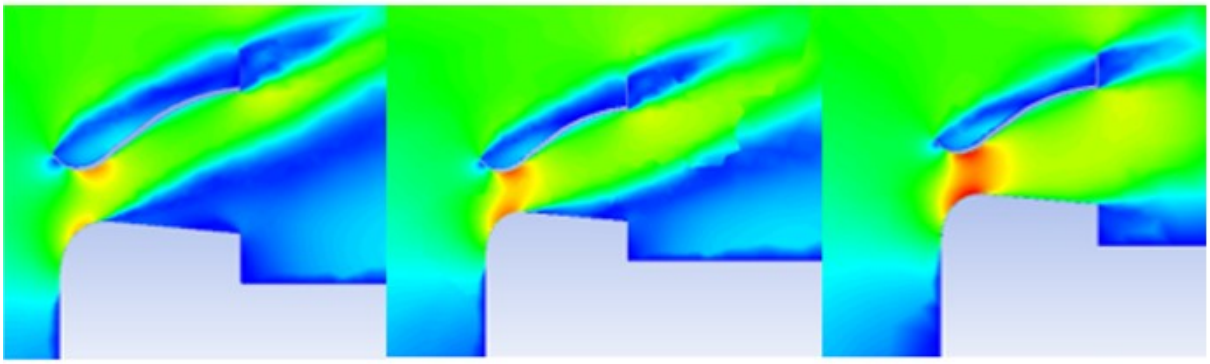

Figure 34 Flow separation with decreasing Reynold number

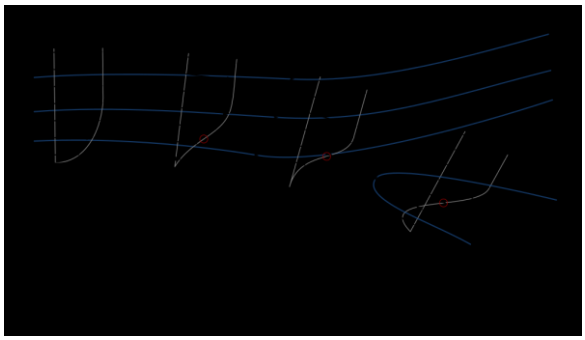

Figure 35 Illustration of flow separation with severe adverse pressure gradient, created by (Cleynen, 2015)

Recognizing the Reynolds number effect on the flow characteristics, an exact geometric scale of the wind tunnel model is also created in CFD for the sole purpose of comparison and validation of the CFD methods. Note that the wind tunnel results may not compare with the full-scale CFD velocity or pressure results (at Re= 17 million) as stated earlier wind tunnel results will likely predict the flow separation. But once the 1:100 scale CFD model results comparison with the wind tunnel results validates the accuracy of the methodology used, the same CFD method can then be used to optimize and predict the performance of the diffuser in a more complex urban environment.

Static pressure along the stream-wise direction on the bottom diffuser shroud is measured using 21 pressure taps in three rows to investigate the pressure variation in the stream-wise as well as the traverse direction. The measured pressure values are then converted to pressure coefficient using dynamic pressure calculated upstream using a pitot tube and scaled for the same height of the diffuser on the rooftop.

5.2.2 Cp comparison in the traverse direction

The pressure coefficients match very closely in traverse direction – see Figure 37 (top) - between the three rows, symmetry, midline, and inner wall. Note that the pressure taps are

located between 0.3 mm from the entrance to 4.5 mm along stream-wise direction. It was physically not possible to install pressure taps any closer to the entrance nor to the outlet. As a result, the expected dip showing the initial acceleration near the entrance is not captured with full picture. Nevertheless, the spike at the entrance of all three rows represents the high speed of the flow at the entrance. The Cp also indicates the slowing down of the airflow as it expands with the increasing size of the opening.

At the first point of the near-wall row at the flow entrance, the pressure coefficient predicts a lower negative pressure or lower wind speed. This is expected as the flow speed is lower near the side wall. CFD results also predict that the boundary layer is thicker near the corner between the bottom shroud and the side wall. Figure 36 shows the front view of the diffuser throat at different locations with the velocity contours, advancing in the stream-wise direction. It can be seen that the boundary layer grows in the stream-wise direction and flow eventually separates. It is more severe near the corner due to the stronger adverse pressure gradient with wall shear stress of the two wall surfaces “resisting” the incoming flow.

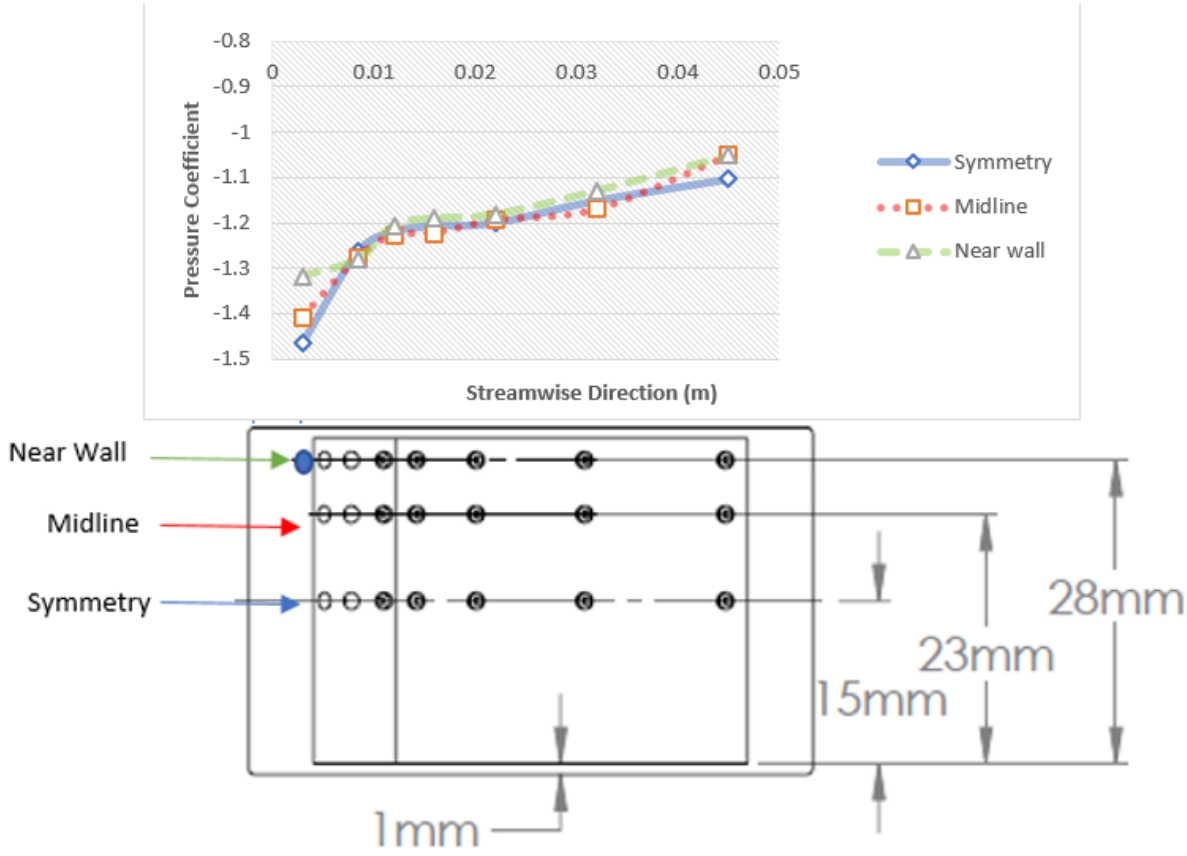

Figure 36 Wind tunnel Cp result comparison in traverse direction (top) and the diffuser geometry and the pressure tap locations (bottom)

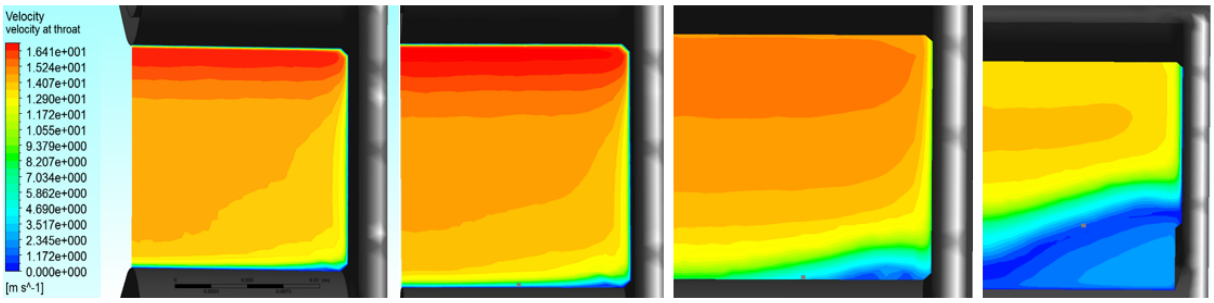

Figure 37 Velocity contour inside the diffuser in stream-wise direction (from left to right velcoity contour cross section view in streamwise direction)

5.2.3 Cp comparison between CFD and wind tunnel results and discussion

Figure 38 shows the comparison of pressure coefficient of CFD results with wind tunnel results.

Note that the figure shows a similar Cp trend along the stream-wise direction in both CFD and

the wind tunnel results but with some discrepancies in the exact values. To fully understand the discrepancy between them, both CFD and the wind tunnel setup were examined with a variety of different setups. A wide range of CFD boundary conditions and different turbulence models were used and in different scales. The wind tunnel experiment was also conducted many times to test consistency of the results. But all the effort trying to debug the possible issue resulted in similar outcome. Possible causes of this discrepancy may be geometric scaling of wind tunnel models (Stathopoulos and Surry, 1983) and the inaccuracy associated with pressure tap measurement in separation flow regions on the bottom shroud.

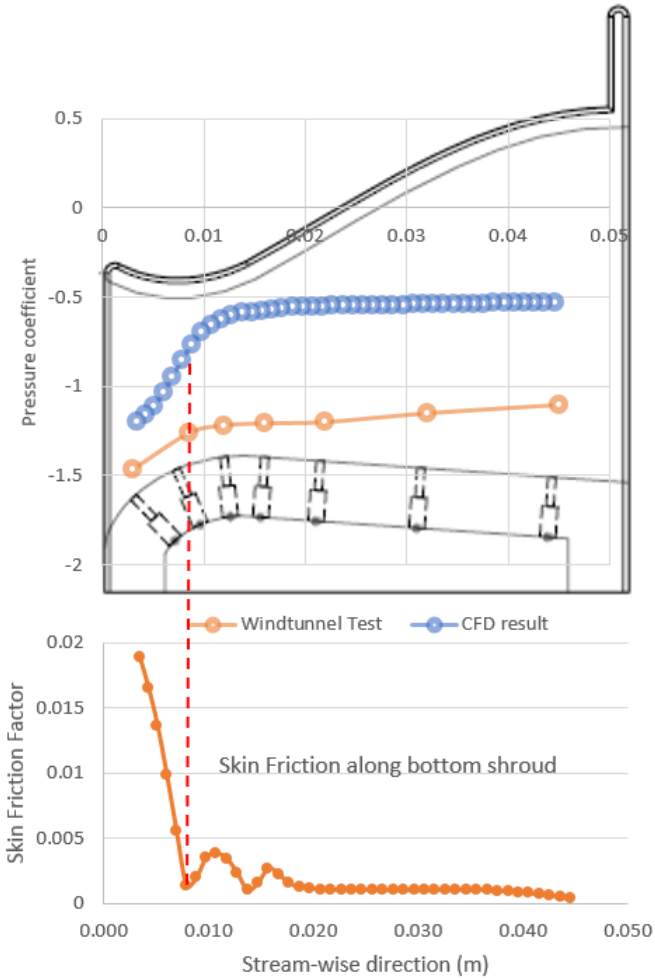

Figure 38 Cp comparison of the CFD and Wind tunnel test results (top) and skin friction factor on the bottom

Wall static pressure taps are often prone to errors in recirculating flow regions. Longer pressure tap holes with high L/d ratio are known to have higher error (McKeon and Smits, 2002), with small eddies trapped inside. Where L is the depth of the pressure tap hole and the d is diameter of the hole. This ratio is 8.5 in this wind tunnel experimental case. Another cause of the eddies in the holes is the burrs on the surface where the taps are installed. Due to the lack of space available to maneuver small drills, the pressure tap holes were 3D printed directly in the model. The model is printed using acrylonitrile butadiene styrene (ABS) material and polished prior to installation. But the smoothness is limited by the material property. The discrepancy of Cp along the bottom shroud, especially after the flow separation point, may be attributed to the inability of the pressure taps to accurately measure the pressure values in regimes where the flow is detached from the wall. The Figure 38 (bottom) shows the skin friction factor, which is calculated from the CFD wall shear stress along bottom shroud surface nondimensionalized by dynamic pressure. The shear stress/ skin friction drops steeply at 0.01 m from the flow entrance. This is due to the flow separation at the surface location. Interestingly, both CFD and wind tunnel Cp results show similar kink and the flattening of the Cp curves after approximately 0.01 m, which is the location where the flow starts to separate.

But the main reason for the gap between the wind tunnel and CFD results is possibly the use of improper geometric scale, which is known to have inherent discrepancy associated with the pressure measurement in the wind tunnel. Stathopoulos and Surry (1983) investigated the effect of the geometric scales in the wind tunnel on the pressure measurements using three different scales, 1:100, 1:250, 1:500. The ideal scale is argued to be at around 1:500. The 1:100 is found to have the largest discrepancy. The recommended geometric scale was not achievable for the previous wind tunnel tests conducted to validate the diffuser CFD results. The diffuser must be

less than a few millimeters in size to meet the requirement. The discrepancy associated with smaller scales such as 1:100 is found to be around 20~30% (Stathopoulos and Surry, 1983). The discrepancy is especially higher on roofs with Cp overprediction of as much as 55% for peak values. Stathopoulos and Surry (1983) argue that the overprediction of the roof pressure coefficient is attributed to the secondary flow regime such as flow separation and eddies of the flow as it goes over the roof. The CFD validation test result shows that the wind tunnel Cp is 22% higher than the CFD result at the inlet until where the flow separates, while in the flow separation region, the wind tunnel overpredicts Cp by approximately 50 %. The inherent overprediction shown by Stathopoulos and Surry (1983) of smaller geometric scale and the overprediction of Cp in the flow separation region can explain the consistent discrepancy between the wind tunnel and the CFD results of the diffuser. Further investigation including implementation of different geometric scales and different Reynolds number must be carried out to further understand this phenomenon. Nevertheless, the Cp result and the extrapolated values of the stream-wise velocity is evident that the diffuser is certainly capable to increasing the wind speed inside the diffuser mechanism.

CHAPTER 6: URBAN WIND ENERGY AND WIND PROFILE ANALYSIS IN BUILT-ENVIRONMENT

Urban wind flow characteristics are highly complex compared to that in wind farms. Urban areas include structures such as buildings so the airflow faces high surface roughness affecting the wind profile significantly. With buildings obstructing the flow path at the lower atmospheric layer, rapid change of flow direction and turbulence intensity are unavoidable. This type of flow contributes to the unpredictability of wind energy in urban areas. Nevertheless, recent research suggests that urban wind energy is a great source of renewable energy though they acknowledge the difficulties associated with implementation (An-Shik Yang et al., 2016a, Morbiato et al., 2014, Toja-Silva et al., 2013). Average wind speed in a built-environment is lower than in rural areas and typical wind farms. Nevertheless, the tunneling effect created between buildings offers higher local wind speeds. Such regions include narrow gaps between tall buildings, like the Bahrain World Trade Center Towers, and the exteriors of high-rise buildings including the edge of the building rooftops. Therefore, the analysis of wind in complex terrains is important for micro-siting of wind turbines (Ledo et al., 2011). One of the main difficulties in deployment of urban wind turbines is the lack of means to accurately predict wind energy potential (An-Shik Yang et al., 2016b). Determining flow field is essential in assessing wind power. Different methods such as Weibull analysis, micrometeorology data, experimental measurement and computational fluid dynamics (CFD) were used to evaluate availability of wind energy for power generation (Chandel et al., 2014, Mertens, 2002). Field measurements and wind tunnel experiments are traditionally the most reliable in such analysis. However, in field measurements as well as in wind tunnel tests only point measurements are performed in selected areas, thus making it great for macro-siting of wind turbines such as wind farms. But for micro-siting of

wind turbines, these measurements are not as convenient. Techniques such as Particle Image Velocimetry (PIV) and Laser-Induced Florescenes (LIF) can provide scan data of 2D or in some cases 3D wind flow profile, but they are very expensive and difficult to perform (Blocken, 2015). Numerical modeling of wind flow in built areas using CFD is a great alternative. With the current day advancement of computing technologies and commercial software, CFD can perform such wind studies much faster and provide greater details at high resolution facilitating the micro-siting of small urban wind turbines. Miller et al., (2013) argues that CFD can provide a good picture of wind characteristics and can be used as a reliable tool in evaluating specific sites. A study conducted by Prospathopoulos et al., (2012) compared results from 3D RANS solver with experimental data. Results show that CFD predicts wind profile in complex terrain accurately except in steep terrains, such as cliffs.

Based on the great number of articles on CFD implementation in urban wind engineering as well as following the specific guidelines and the best practices of modeling atmospheric boundary layer flows in urban environments by Blocken et al., 2004, Blocken and Carmeliet, 2004, Blocken et al., 2007, Blocken et al., 2011, Blocken, 2015, Franke et al., 2011 and Toparlar et al., 2015, CFD tests are performed to improve the deployment of rooftop-mounted urban wind turbines by introducing an external turbine casing mechanism – a diffuser shroud, on the rooftop of a test building, for its ability to utilize the incoming flow over the edge of a building rooftop. The diffuser shroud, a fluid machine, sitting on the roof of a tall building, guides the upward climbing airflow and further accelerates the flow inside the diffuser where a small turbine can be installed to harness the wind energy. Analysis using CFD is performed on two test sites in Montreal, Canada to characterize the urban wind flow and to select a siting location for the diffuser. In parallel, a CFD model of the diffuser on a hypothetical single building case is created for geometric analysis and the optimization of the diffuser performance. Then with

the optimized diffuser shroud modeled on the roof of a selected building in one of the test sites, further CFD is performed to show the diffuser's performance as a proof of concept in an attempt to address the challenges faced by the urban wind turbines thus improving urban wind energy systems.

6.1 **Urban wind characteristic study in test sites**

Having to navigate around urban structures such as buildings, wind flow loses much of its power making it difficult to harness useful wind energy. However, careful investigation of wind flow profile over the building rooftop brought to attention the possibilities of taking advantage of such flow patterns. Two different urban test sites, one in the Cote-des-Neiges borough of Montreal, located in a residential area with dense urban structures, such as apartment buildings and trees (1) and another in Pointe-Claire, Quebec, a commercial area with shopping malls and big open parking lots around the core domain (2) – see Figure 39.

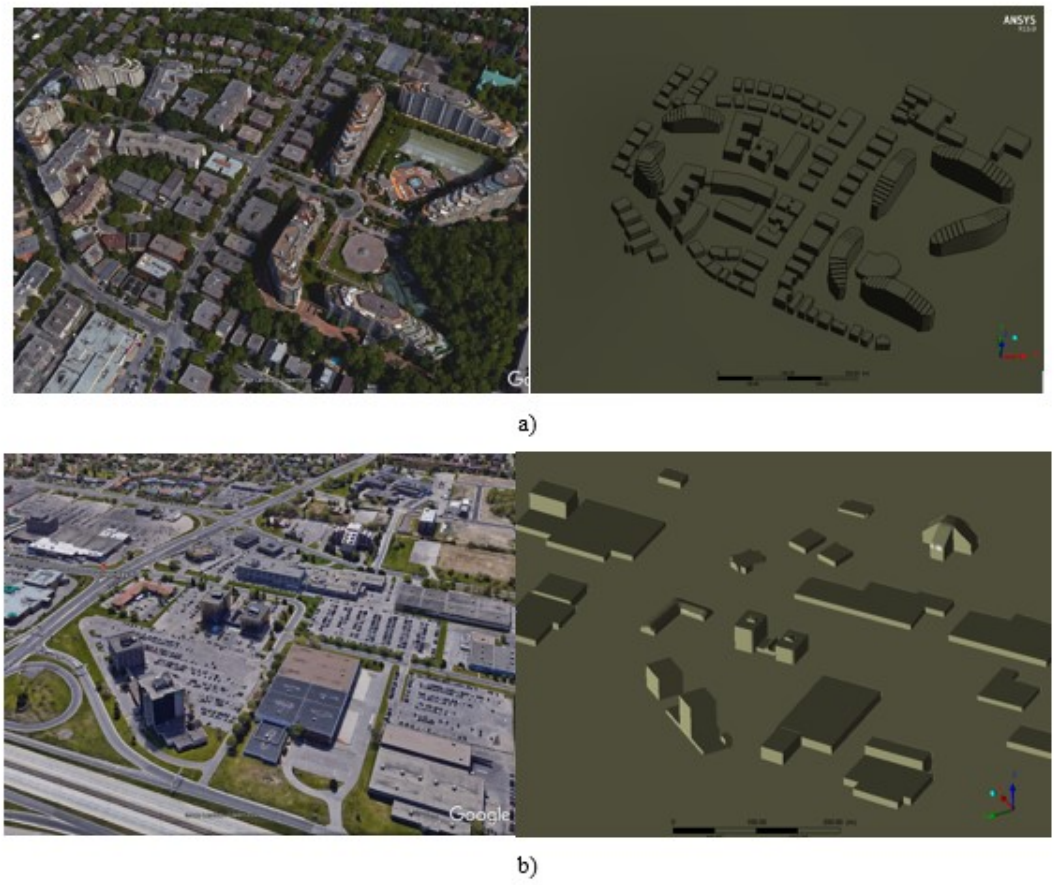

Figure 39 a) Test site in the Cote-des-Neige borough of Montreal, Canada, Google Earth view (left), model geometry (right), b) Test site in a commercial area in Pointe-Claire, Quebec, Canada, Google Earth view (left), model geometry (right)

6.2 **Computational domain**

CFD simulation was performed for eight different wind directions with an azimuthal increment angle of 45 degrees in both test sites. For consistency, only one mesh is created for each test site and only the boundary conditions such as wind direction is modified. The area of interest or the core domain is approximately a rectangular area, 500 meters in each side. The core domain is extended and an octagonal prismed domain with eight lateral sides is created with 500 meters height from the ground to the top, and 2000 meters from the inlet to the outlet – see Figure 40 (a). This will allow the core domain to have a downstream domain extension of approximately 15H where H is the height of the tallest building in the test site, 15H in the lateral

sides, and 10H in vertical height. Figure 40 (a) shows the domain geometry and the (b) shows the computational domain as well as the ground topography. Unstructured mesh with fine inflation layers, 5 layers within the 2 meters height, on the ground is created to accurately capture the flow gradients near the ground surface. The inflation layers near the ground surface are triangular prism mesh. Figure 41 illustrates the surface mesh on the buildings and the ground.

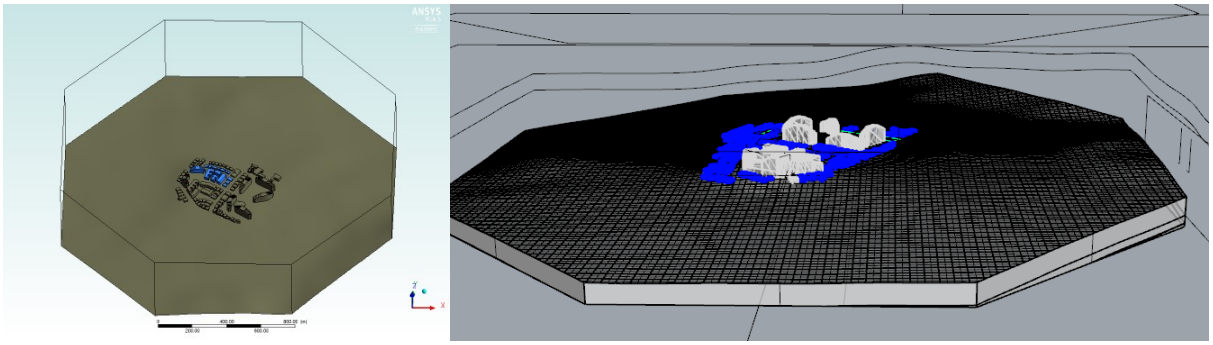

a) b)

Figure 40 a) Computational domain, b) ground topography

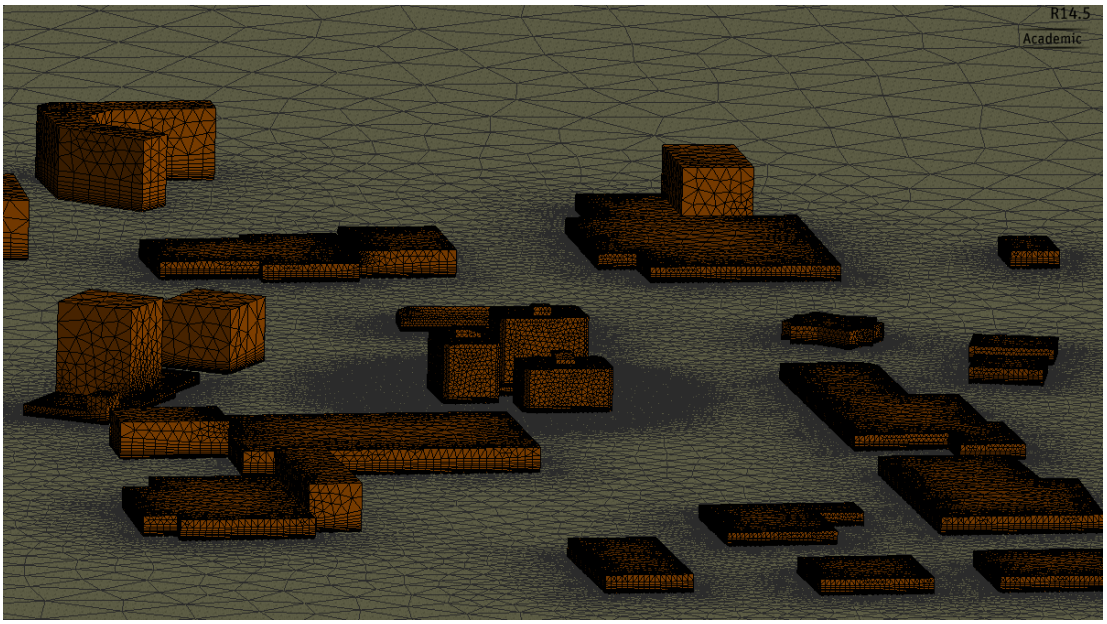

Figure 41 Mesh for test site Point-Claire, Montreal

6.3 **Boundary conditions for ABL flow profile**

Three of the eight vertical side faces are used as velocity inlet with boundary conditions defined by equations 6.2 to 6.4 to apply velocity and turbulence parameters such as k and ε to realistically capture urban atmospheric boundary layer flow. The opposite three sides are defined as pressure outlet in each one of the eight wind direction cases, while the remaining two sides and the top are modelled as symmetric boundary condition – see Figure 42. Figure 43 shows the ABL velocity profile at the domain inlet. The u^*_{ABL} is the ABL friction velocity used to determine turbulent kinetic energy, k and the turbulent dissipation, ε. K is the von Karman constant and C_u is a model constant of the turbulence model. The z is the domain z coordinate representing the vertical elevation. The core domain geometric details where the buildings are located are explicitly modeled and the beyond the core domain such as upstream, sides, and the downstream sections are implicitly modeled using aerodynamic roughness z_0 and the roughness height k_{sABL} to account for the roads, buildings, and the vegetation outside of the core domain. The relationship between z_0 and $k_{s,ABL}$ are shown in equation 6.1 and incorporated into the solution process. Realizable k-ε turbulence modelling has demonstrated superior performance for simulation that involves flow separation, vortex eddies and recirculation (Karava et al., 2011). Standard incompressible Navier-Stokes equations 2.1 and 2.2 with Ansys FLUENT 3D steady state model are used with the Realizable k-ε turbulence modelling.

$$k_{S,ABL} = \frac{9.793\, z_0}{C_s} \tag{6.1}$$

$$U_{ABL} = \frac{u^*_{ABL}}{K} In\,(\frac{z+z_0}{z_0}) \tag{6.2}$$

$$k = \frac{(u^*_{ABL})^2}{\sqrt{C_u}} \tag{6.3}$$

$$\varepsilon = \frac{(u^*_{ABL})^3}{K(z+z_0)} \tag{6.4}$$

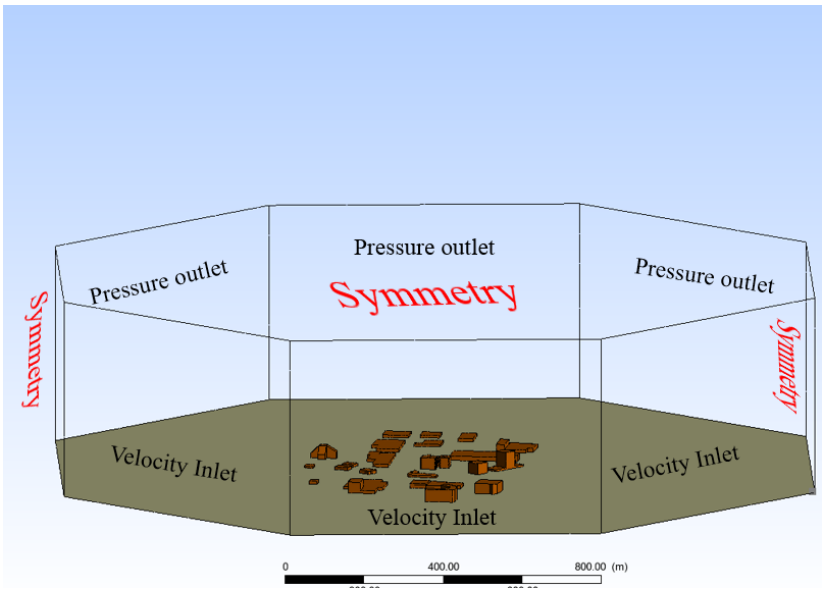

Figure 42 Domain and boundary conditions

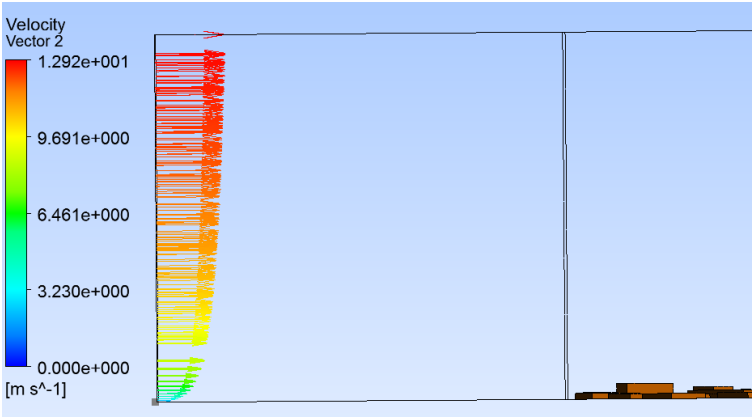

Figure 43 Velocity profile at the inlet of the domain

6.4 **Summary of findings in test sites**

The preliminary CFD analysis shows that the wind profile is very complex in built-environment such as the test sites. Figure 44 (a) and (b) show the velocity streamlines of the flow in the test site (2) and (1) respectively, in which, the local flow profile changes significantly with each

different wind direction and the flow is highly turbulent due to dense topographical structures. The mean wind speed is low for meaningful power generation. There are large vortices in between buildings that may affect the stability of any local flow acceleration such as flow over the roof. There are buildings with different shapes and roofs. The building geometry and the roof shape also play an important role in shaping wind flow. Complexity of the flow pattern and the turbulence is more forgiving in test site (2) with large open areas such as grass and parking lots near the core domain. Some of the important factors to consider when selecting a turbine site are:

- Wind direction with respect to the building geometry;
- Building height in relation to surrounding structures;
- Spacing of the buildings;
- Upstream topography and its effect on the ABL profile;
- Shape of the buildings and the roofs.

Flow pattern shown in Figure 45 (a) in test site (1), the velocity vector of the flow upstream of a building, is similar to that in test site (2) – see Figure 46 (a). Figure 46 (b) illustrates a smoke visualization of airflow over two buildings in a wind tunnel from an ABL flow study performed by Blocken and Carmeliet (2004). The smoke visualization shows that when the surrounding buildings are relatively lower and certain distance apart, upper flow layer climbs upward as it approaches tall buildings and accelerates. The upward flow is dependent on the flow direction with respect to the roof and flows higher over the rooftop. Similar pattern of airflow is observed in CFD results -See Figure 45 (a) and Figure 46 (a). Wineur project and Warwick wind trials (2009) recommend that any roof-mounted wind turbine should be installed at a location 30% higher of the building height because of the turbulence region at the lower level of the flow

over the roof. If the upward airflow can be guided, the acceleration can be beneficial for power generation; and perhaps the costs and complications associated with installing large turbine towers on the rooftops can be avoided.

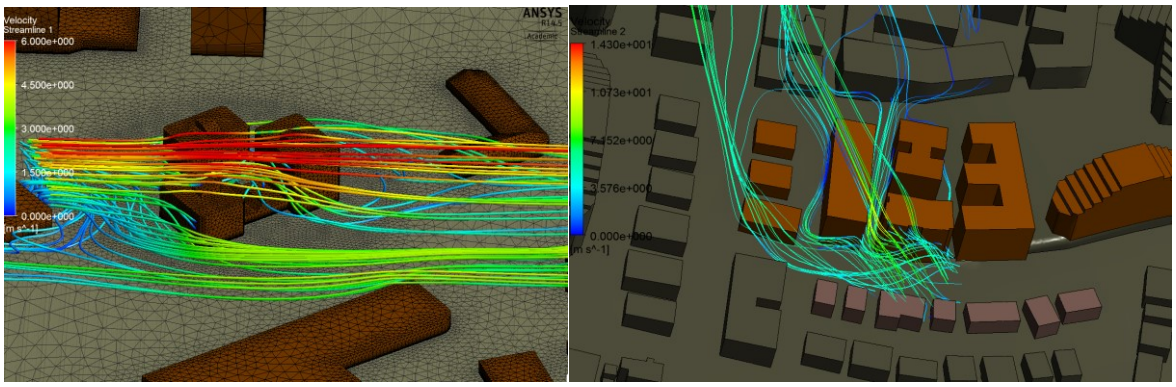

a) b)

Figure 44 Velocity streamlines in in the test sites a) test site (1), Cote-des-Neiges b) test site (2), Point-Claire

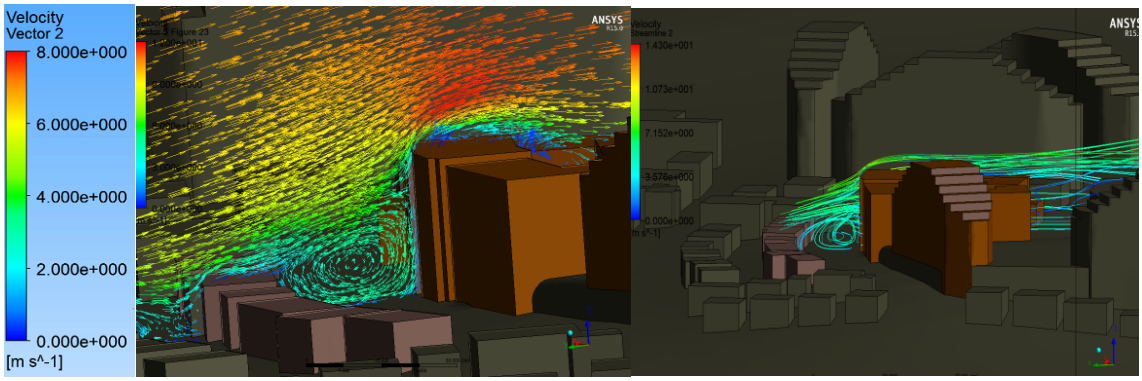

a) b)

Figure 45 Flow over building roof in test site (1) a) CFD velocity vector b) CFD velocity streamlines

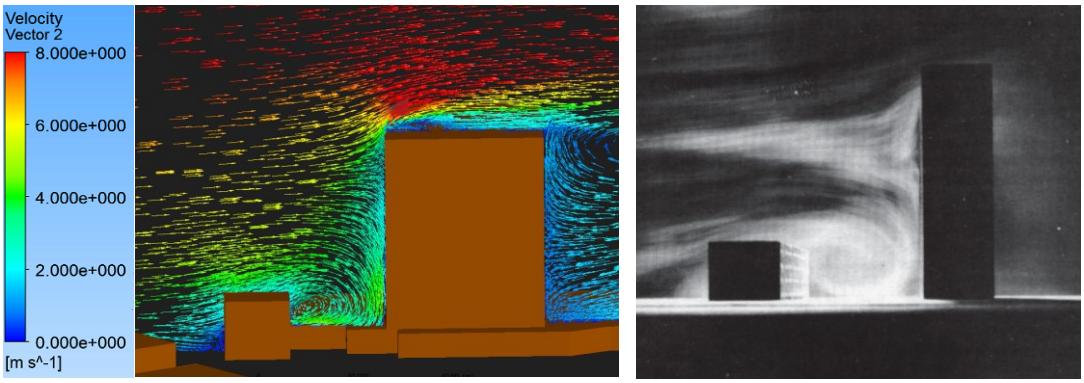

a) b)

Figure 46 a) Velocity vectors in test site (2) b) smoke visualization of flow in wind tunnel (Blocken and Carmeliet, 2004)

CHAPTER 7: DIFFUSER SHROUD MECHANISM MODELLING IN THE TEST SITE

One of the challenges and skepticism of optimization of a specific design is that the performance improvement may be dependent on the setup of the diffuser including its location, as it is specific to local flow characteristics. So before going into too much fine-tuning, it is important to verify the performance of the diffuser in an existing urban environment. A CFD analysis is carried out to test the mechanism on a rooftop of an existing building in the test site to further verify its performance promised by the previous CFD investigation.

7.1 **Diffuser performance on the roof of test building**

To further verify if the diffuser shroud performance is realistic in real urban areas, a CFD analysis is performed to test the mechanism on a rooftop of an existing urban structure in test site (2). To ease some of the difficulties in mesh creation and the computational costs associated having to create much finer mesh with k-ω SST turbulence model for the much larger and complex domain, the Realizable k-ε turbulence model is used instead in this stage. The realizable k-ε turbulence model showed very close results compared to the baseline k ω SST model in the previous CFD analyses. Wind roses with wind statistics of Montreal including dominant wind directions are used as input for the boundary conditions of CFD setup following the best practices recommended by Blocken (2015). Based on the statistical dominant wind direction, westerly wind – see Figure 49 for wind rose in Montreal; the location advantage, such as, being the tallest building with less dense structures in the immediate surrounding, and one of the building sides facing directly west, the building encircled in yellow – see Figure 46 – in test site (2) is chosen as the test building. Figure 46 (b) shows the numerical model of the building with the diffuser modeled on the rooftop and (a) the google earth view of the location.

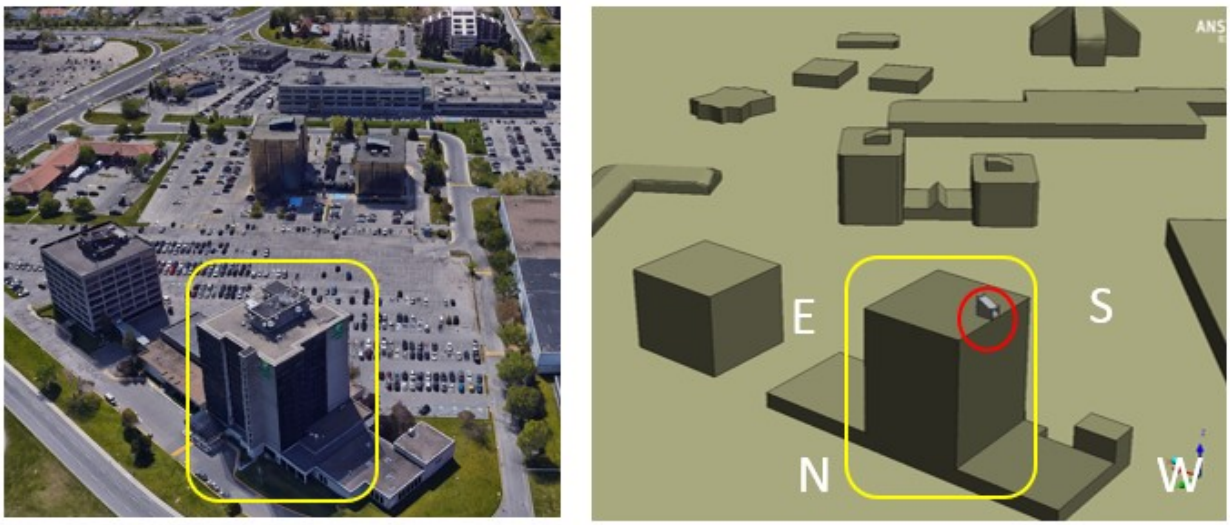

a) b)

Figure 47 Selected building in the test site in Point-Claire, Quebec

a) Google Earth view b) CFD model

The CFD results of the test site agree well with the prediction of the design stage CFD for performance of the diffuser. The test site CFD shows that the velocity is magnified by 1.52 times at the throat of the diffuser. Figure 48 shows (a) velocity contours at the cut plane of the diffuser and 48 (b) velocity streamlines at the selected building with the diffuser on top. This is very close to the result of 1.6 predicted by the CFD results from the design stage– see Figure 29 (a). The velocity is calculated as the mass flow average at the diffuser throat and compared to the velocity upstream at the same height. The flow coming from west (left in Figure 47) approaches the building and the upper flow layer moves upward over the edge. This airflow is drawn into the diffuser with the suction created by the flange at the outlet, sharply bending the flow direction. The flow pattern near the selected building without the diffuser – see Figure 46 (a) - is similar to that in the model with the diffuser – see Figure 48 (b). The streamlines shown in red – see Figure 47 (b) – right at the diffuser inlet indicates that the flow accelerates going into the diffuser. The diffuser on the test building effectively takes advantage of the local flow

acceleration as predicted in the design stage. The increased wind speed with the help of the diffuser mechanism translates to a power increase of a 3.51 times of a wind turbine that is installed at the same height on a tower.

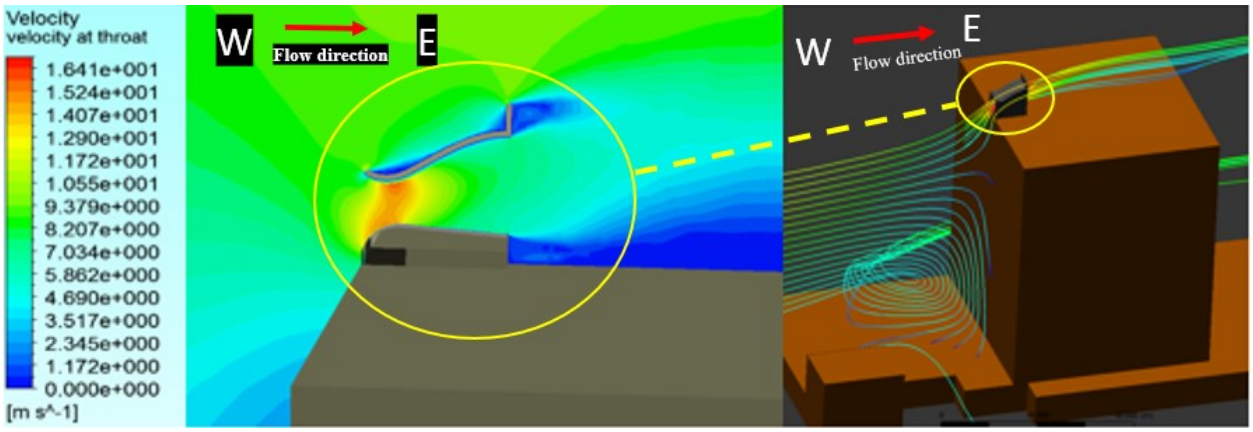

a) b)

Figure 48 a) velocity contour at the diffuser cut plane b) velocity streamlines in perspective view of selected building

7.2 **Diffuser performance with varying wind direction in test site**

In addition to the westerly wind, azimuthal angle of 270 degrees, two other cases with azimuthal angle of 225 (SW) and 247.5 degrees (WSW) are tested to examine the diffuser's performance in different wind directions. Result shows that diffuser does not perform well with SW with 45 degrees offset. Table 8 summarizes the velocity magnification factors in three wind directions. One of the reasons is the flow disturbance upstream with other buildings. WSW case predicts a velocity magnification of 1.7 which is even higher than the W wind case where wind flow is facing the diffuser inlet. After investigation, it became clear that this increase in flow speed is due to the special geometry the airflow faces in the WSW case. Air accelerates more around the building first by splitting at the corner and at the edge of the building. It then flows upwards over the roof getting accelerated once more – see Figure 50 - before getting drawn into the diffuser as oppose to having to turn 90 degrees upwards to go over the roof in the westerly wind

case where the wind faces the diffuser inlet directly. The flow creates significant eddies behind the shroud structure in WSW. This will create unsteady disturbance to the flow inside the diffuser. Airflow seems to "bend" into the diffuser just as it goes over the roof. This acceleration is certainly beneficial for power generation. But the flow in this configuration should be investigated further to better understand the stability of the flow magnification. Figure 51 (a) and (b) show the velocity streamlines upstream of the diffuser mechanism in WSW and W cases respectively.

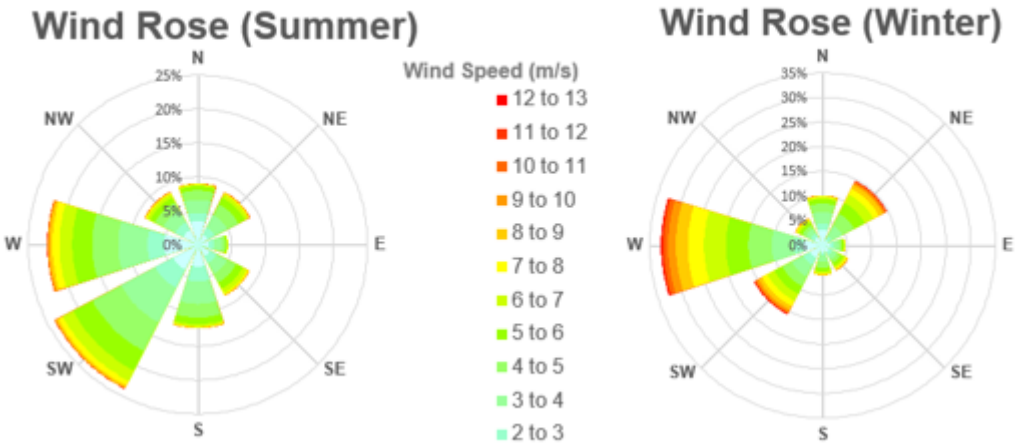

Figure 49 Wind Roses in Montreal

Table 8 Velocity magnification factor

Wind Direction	**Azimuthal Angle**	$\frac{U}{U_\infty}$
W	270	1.52
SW	225	≤ 1
WSW	247.5	1.7

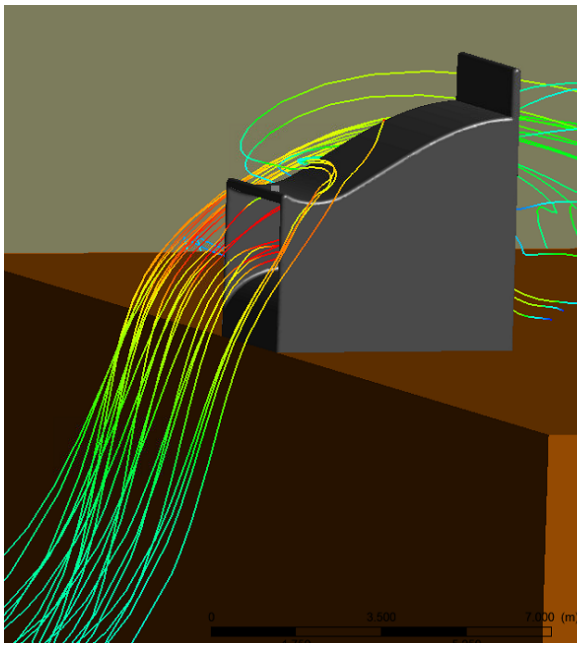

Figure 50 Velocity streamlines for WSW case in test site (2)

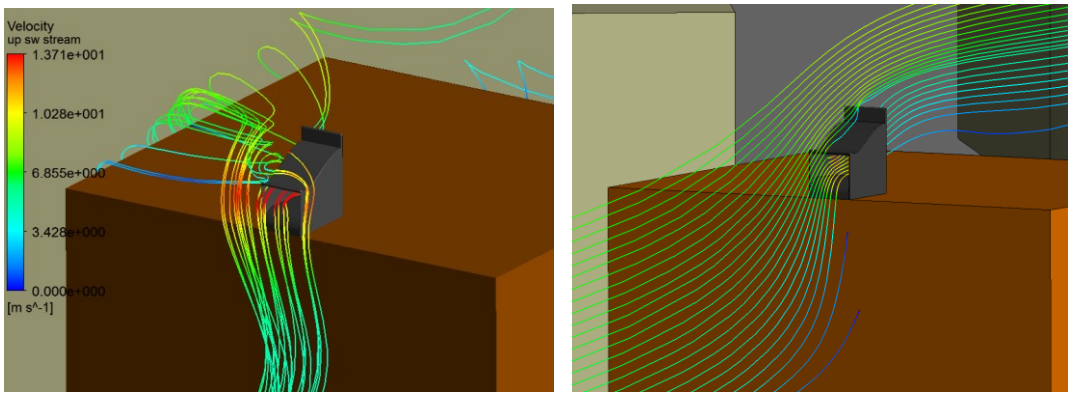

a) b)

Figure 51 a) WSW wind velocity streamlines b) West wind velocity streamlines

CHAPTER 8: CONCLUSION

8.1 **Summary**

The scarcity of experimental data of wind turbines installed in urban settings makes it harder to compare turbine efficiencies as well as the viability of different wind turbines available today. Conventional wind turbines directly implemented in urban built-environment do not perform well. Some wind turbines, especially VAWTs, still show good results but should be further optimized for urban applications. Power augmentation concepts using diffuser and shrouded brims around conventional wind turbines promise significant power coefficient increase. The flanged shrouded diffuser mechanism can re-direct the airflow over building rooftop towards the wind turbine installed inside of the diffuser casing as well as can accelerate the flow augmenting wind power. In most cases, small wind turbines in urban setting do not generate meaningful power output due to many reasons, the low cut-in speed being the one of them. The fluid machine directly addresses this problem by increasing the wind speed significantly.

CFD investigation of the concept proves very promising. With the increased wind speed inside the casing, the diffuser mechanism can increase urban wind turbine efficiency by up to 4 times compared to conventional wind turbines. Wind tunnel tests are performed to validate the CFD results. The challenges associated with the Reynolds number similarity and the effect of geometric scales in wind tunnels are significant thus creating some challenges for the validation process. Nevertheless, the pressure data measured in the wind tunnel shows that the diffuser is indeed capable of accelerating the flow inside the diffuser casing.

The fluid machine performed well on a rooftop in a real test site. CFD predicts the velocity magnification factor to be closely matched between the concept design stage (chapter 4) and

the test site deployment (Chapter 7). The mechanism can function moderately well with different wind angles. The test site CFD analysis shows that the fluid machine can guide wind flows from azimuthal angle range of at least $\pm$ 22.5 degree, totaling 45 degrees in range.

The performance of the shrouded diffuser mechanism is dependent on factors such as, turbulence and velocity profile specific to the location of interest. Guidelines and best practices of CFD used to simulate ABL flow in built-environment must be followed to accurately capture the ABL flow characteristics. Site-specific wind profile analysis together with rooftop turbulence assessment can significantly improve the performance of this mechanism thus improve turbine efficiency. The Reynolds number effect is significant on the flow structure near the buildings. This can adversely affect the performance of the diffuser. Tall buildings with flat roofs are ideal for implementation of this fluid machine.

Exploiting shrouded power augmentation technologies and proper synergistic design of turbines and buildings, urban wind power extraction can become an important part of renewable energy source. Urban wind turbine technology is still at its early state and there is a lot of space to improve- promising directions have already been identified. There are still a lot of questions about the performance of wind turbines and its economics but continuous research in this area will provide some of the much-needed answers.

8.2 **Future work**

The challenges with wind tunnel tests to validate the CFD results should be examined more in depth. Certain measures can address the Reynolds number similarity issue and circumvent the challenges in wind tunnel experiments by artificially modifying the flow profile and mimicking higher Reynolds number flow characteristics.

Due to the time-consuming nature of wind tunnel experiments, only one geometric scale of the model is tested. To better understand the flow separation at the curved surfaces of the diffuser bottom shroud, different geometric scales should be investigated in the wind tunnel.

Reynolds number and the reference velocity applied at the inlet boundary condition are significant factors that can alter the flow pattern in the diffuser shroud mechanism. A case specific analysis should be carried out before deployment of the mechanism.

REFERENCES

Encraft Warwick Wind Trials Final Report2009. 2016, 64.

Abohela, I., Hamza, N., Dudek, S. 2013. Effect of roof shape, wind direction, building height and urban configuration on the energy yield and positioning of roof mounted wind turbines. Renewable Energy 50, 1106-18.

Ani, S.O., Polinder, H., Ferreira, J.A. 2013. Comparison of Energy Yield of Small Wind Turbines in Low Wind Speed Areas. IEEE Transactions on Sustainable Energy 4, 42-9.

An-Shik Yang, Ying-Ming Su, Chih-Yung Wen, Yu-Hsuan Juan, Wei-Siang Wang, Chiang-Ho Cheng. 2016a. Estimation of wind power generation in dense urban area. Applied Energy 171, 213-30.

An-Shik Yang, Ying-Ming Su, Chih-Yung Wen, Yu-Hsuan Juan, Wei-Siang Wang, Chiang-Ho Cheng. 2016b. Estimation of wind power generation in dense urban area. Applied Energy 171, 213-30.

Ansys, F. 2011. ANSYS FLUENT 14.0 Theory Guide. www.fluent.com 2016.

Ashwill, T.D., Veers, P.S. 1990. Structural response measurements and predictions for the Sandia 34-meter test bed 9, 137-144.

Balduzzi, F., Bianchini, A., Carnevale, E.A., Ferrari, L., Magnani, S. 2012. Feasibility analysis of a Darrieus vertical-axis wind turbine installation in the rooftop of a building. Applied Energy 97, 921-929.

Batista, N.C., Melicio, R., Mendes, V.M.F., Calderon, M., Ramiro, A. 2015. On a self-start Darrieus wind turbine: Blade design and field tests. Renewable and Sustainable Energy Reviews 52, 508-522.

Belkacem, B., Paraschivoiu, M. 2016. CFD Analysis of a Finite Linear Array of Savonius Wind Turbines 753.

Bilir, L., Imir, M., Devrim, Y., Albostan, A. 2015. An investigation on wind energy potential and small scale wind turbine performance at Incek region - Ankara, Turkey. Energy Conversion and Management 103, 910-23.

Blocken, B., Roels, S., Carmeliet, J. 2004. Modification of pedestrian wind comfort in the Silvertop Tower passages by an automatic control system. Journal of Wind Engineering and Industrial Aerodynamics 92, 849-73.

Blocken, B. 2015. Computational Fluid Dynamics for urban physics: Importance, scales, possibilities, limitations and ten tips and tricks towards accurate and reliable simulations. Building and Environment 91, 219-245.

Blocken, B., Carmeliet, J. 2004. Pedestrian wind environment around buildings: Literature review and practical examples. Journal of Thermal Envelope and Building Science 28, 107-159.

Cace, J., Horst, E., Syngellakis, K., Niel, M., Clement, P., Heppener, R., Peirano, E. 2007. Urban Wind Turbines, Guidelines for small wind turbines in the built environment 2016, 41.

Chandel, S.S., Ramasamy, P., Murthy, K.S.R. 2014. Wind power potential assessment of 12 locations in western Himalayan region of India. Renewable and Sustainable Energy Reviews 39, 530-545.

Chong, W.T., Fazlizan, A., Poh, S.C., Pan, K.C., Hew, W.P., Hsiao, F.B. 2013. The design, simulation and testing of an urban vertical axis wind turbine with the omni-direction-guide-vane. Applied Energy 112, 601-609.

Chong, W.T., Poh, S.C., Fazlizan, A., Pan, K.C. 2012. Vertical axis wind turbine with omni-directional-guide-vane for urban high-rise buildings. Journal of Central South University of Technology 19, 727-32.

Cleynen, O. 2015. Boundary layer separation, https://commons.wikimedia.org/wiki/File:Boundary_layer_separation.svg 2017, 1.

D'Ambrosio, M., Medaglia, M. 2010. Vertical Axis Wind Turbines: History, Technology and Applications.

Danao, L.A., Eboibi, O., Howell, R. 2013. An experimental investigation into the influence of unsteady wind on the performance of a vertical axis wind turbine. Applied Energy 107, 403-411.

Drachmann, A.G. 1961. Heron's Windmill, in: Heron's Windmill, 145-151. Centaurus.

Elkhoury, M., Kiwata, T., Aoun, E. 2015. Experimental and numerical investigation of a three-dimensional vertical-axis wind turbine with variable-pitch. Journal of Wind Engineering & Industrial Aerodynamics 139, 111-23.

Eriksson, S., Bernhoff, H., Leijon, M. 2008. Evaluation of different turbine concepts for wind power. Renewable and Sustainable Energy Reviews 12, 1419-1434.

Franke, J., Hellsten, A., Schlunzen, K.H., Carissimo, B. 2011. The COST 732 Best Practice Guideline for CFD simulation of flows in the urban environment: A summary. International Journal of Environment and Pollution 44, 419-427.

Glass, A., Levermore, G. 2011. Micro wind turbine performance under real weather conditions in urban environment. Building Services Engineering Research & Technology 32, 245-62.

Govindharajan, R., Parammasivam, K.M., Vishnu Priya, R. 2013. NUMERICAL INVESTIGATION AND DESIGN OPTIMIZATION OF BRIMMED DIFFUSER – WIND LENS AROUND A WIND TURBINE. The Eighth Asia-Pacific Conference on Wind Engineering.

Grieser, B., Sunak, Y., Madlener, R. 2015. Economics of small wind turbines in urban settings: an empirical investigation for Germany. Renewable Energy 78, 334-50.

Kadar, P. 2012. Comparative performance analysis of small scale wind turbines. Journal of Engineering Science and Technology Review 5, 42-47.

Karava, P., Jubayer, C.M., Savory, E. 2011. Numerical modelling of forced convective heat transfer from the inclined windward roof of an isolated low-rise building with application to photovoltaic/thermal systems. Applied Thermal Engineering 31, 1950-1963.

Kosasih, B., Saleh Hudin, H. 2016. Influence of inflow turbulence intensity on the performance of bare and diffuser-augmented micro wind turbine model. Renewable Energy 87, 154-167.

Kosasih, B., Tondelli, A. 2012. Experimental Study of Shrouded Micro-Wind Turbine. Procedia Engineering 49, 92-98.

Krishnan, A., Paraschivoiu, M. 2015. 3D analysis of building mounted VAWT with diffuser shaped shroud. Sustainable Cities and Society.

Larin, P., Paraschivoiu, M., Aygun, C. 2016. CFD based synergistic analysis of wind turbines for roof mounted integration. Journal of Wind Engineering & Industrial Aerodynamics 156, 1-13.

Ledo, L., Kosasih, P.B., Cooper, P. 2011. Roof mounting site analysis for micro-wind turbines. Renewable Energy 36, 1379-91.

Lubitz, D., Hakimi, R. 2014. Wind environment at a roof-mounted wind turbine on a peaked roof building. International Journal of Sustainable Energy 35, 172-189.

Macpherson, R.B. 1972. Development and Testing of Low-head High-Efficiency Kinetic Energy Machines -An Alternative for the Future.

Manwell, J.F., Mcgowan, J.G., Roger, A.L. 2002. Wind Energy Explained: Theory, Design and Application. John Wiley and Sons Ltd, Chichester, United Kingdom.

McKeon, B.J., Smits, A.J. 2002. Static pressure correction in high Reynolds number fully developed turbulent pipe flow. Measurement Science & Technology 13, 1608-14.

Mertens, S. 2002. Wind energy in urban areas: Concentrator effects for wind turbines close to buildings. Refocus 3, 22-24.

Miller, A., Chang, B., Issa, R., Chen, G. 2013. Review of computer-aided numerical simulation in wind energy. Renewable and Sustainable Energy Reviews 25, 122-34.

Modi, V.J., Roth, N.J., Fernando, M.S.U.K. 1984. Optimum-configuration studies and prototype design of a wind-energy-operated irrigation system. Journal of Wind Engineering and Industrial Aerodynamics 16, 85-96.

Morbiato, T., Borri, C., Vitaliani, R. 2014. Wind energy harvesting from transport systems: A resource estimation assessment. Applied Energy 133, 152-68.

Morgan, C.A., Gardner, P., Mays, I.D., Anderson, M.B. 1989. The demonstration of a stall regulated 100 kW vertical axis wind turbine, 645-9.

Muljadi, E., Pierce, K., Migliore, P. 1998. Control strategy for variable-speed, stall-regulated wind turbines 3, 1710-1714.

Newman, B.G. 1983. ACTUATOR-DISC THEORY FOR VERTICAL-AXIS WIND TURBINES. Journal of Wind Engineering and Industrial Aerodynamics 15, 347-355.

Nishimura, A., Ito, T., Kakita, M., Murata, J., Ando, T., Kamada, Y., Hirota, M., Kolhe, M. 2014. Impact of building layouts on wind turbine power output in the built environment: A case study of tsu city. Nihon Enerugi Gakkaishi/Journal of the Japan Institute of Energy 93, 315-322.

Ohya, Y., Uchida, T., Karasudani, T., Hasegawa, M., Kume, H. 2012. Numerical studies of flow around a wind turbine equipped with a flanged-diffuser shroud using an actuator-disk model. Wind Engineering 36, 455-72.

Ohya, Y., Karasudani, T. 2010. A shrouded wind turbine generating high output power with wind-lens technology. Energies 3, 634-649.

Ohya, Y., Karasudani, T., Sakurai, A., Abe, K., Inoue, M. 2008. Development of a shrouded wind turbine with a flanged diffuser. Journal of Wind Engineering and Industrial Aerodynamics 96, 524-539.

Pagnini, L.C., Burlando, M., Repetto, M.P. 2015. Experimental power curve of small-size wind turbines in turbulent urban environment. Applied Energy 154, 112-21.

Paraschivoiu, I. 2002. Wind turbine design with emphasis on Darrieus concept. Polytechnic International Press, Canada.

Park, J., Jung, H., Lee, S., Park, J. 2015. A new building-integrated wind turbine system utilizing the building. Energies 8, 11846-11870.

Patankar, B., Tyagi, R., Kiss, D., Suma, A.B. 2016. Evaluation of an Integrated Roof Wind Energy System for urban environments. Journal of Physics: Conference Series 753, 102007 (11 pp.).

Peace, S. 2004. Another approach to wind. Mechanical Engineering 126, 28.

Prospathopoulos, J.M., Politis, E.S., Chaviaropoulos, P.K. 2012. Application of a 3D RANS solver on the complex hill of Bolund and assessment of the wind flow predictions. Journal of Wind Engineering and Industrial Aerodynamics 107-108, 149-59.

Ragheb, M. 2012. Wind turbines in the urban environment 2016, 16.

Rolland, S., Newton, W., Williams, A.J., Croft, T.N., Gethin, D.T., Cross, M. 2013a. Simulations technique for the design of a vertical axis wind turbine device with experimental validation. Applied Energy 111, 1195-203.

Rolland, S.A., Thatcher, M., Newton, W., Williams, A.J., Croft, T.N., Gethin, D.T., Cross, M. 2013b. Benchmark experiments for simulations of a vertical axis wind turbine. Applied Energy 111, 1183-1194.

Roy, S., Saha, U.K. 2015. Wind tunnel experiments of a newly developed two-bladed Savonius-style wind turbine. Applied Energy 137, 117-125.

Saha, U.K., Thotla, S., Maity, D. 2008. Optimum design configuration of Savonius rotor through wind tunnel experiments. Journal of Wind Engineering and Industrial Aerodynamics 96, 1359-1375.

Sharpe, T., Proven, G. 2010. Crossflex: Concept and early development of a true building integrated wind turbine. Energy and Buildings 42, 2365-2375.

Shikha, Bhatti, T.S., Kothari, D.P. 2005. Early development of modern vertical and horizontal axis wind turbines: a review. Wind Engineering 29, 287-99.

Stathopoulos, T., Surry, D. 1983. SCALE EFFECTS IN WIND TUNNEL TESTING OF LOW BUILDINGS. Journal of Wind Engineering and Industrial Aerodynamics 13, 313-326.

Tabassum, S.A., Probert, S.D. 1987. VERTICAL-AXIS WIND TURBINE: A MODIFIED DESIGN. Applied Energy 28, 59-67.

Toja-Silva, F., Colmenar-Santos, A., Castro-Gil, M. 2013. Urban wind energy exploitation systems: Behaviour under multidirectional flow conditions-Opportunities and challenges. Renewable and Sustainable Energy Reviews 24, 364-78.

Touryan, K.J., Strickland, J.H., Berg, D.E. 1987. ELECTRIC POWER FROM VERTICAL-AXIS WIND TURBINES. Journal of Propulsion and Power 3, 481-493.

Wang, W., Matsubara, T., Hu, J., Odahara, S., Nagai, T., Karasutani, T., Ohya, Y. 2015. Experimental investigation into the influence of the flanged diffuser on the dynamic behavior of CFRP blade of a shrouded wind turbine. Renewable Energy 78, 386-397.

Wright, A.K., Wood, D.H. 2004. The starting and low wind speed behaviour of a small horizontal axis wind turbine. Journal of Wind Engineering and Industrial Aerodynamics 92, 1265-1279.

Yan-Fei Wang, Mao-Sheng Zhan. 2015. Effect of barchan dune guide blades on the performance of a lotus-shaped micro-wind turbine. Journal of Wind Engineering & Industrial Aerodynamics 136, 34-43.